



저작자표시-비영리-변경금지 2.0 대한민국

이용자는 아래의 조건을 따르는 경우에 한하여 자유롭게

- 이 저작물을 복제, 배포, 전송, 전시, 공연 및 방송할 수 있습니다.

다음과 같은 조건을 따라야 합니다:



저작자표시. 귀하는 원저작자를 표시하여야 합니다.



비영리. 귀하는 이 저작물을 영리 목적으로 이용할 수 없습니다.



변경금지. 귀하는 이 저작물을 개작, 변형 또는 가공할 수 없습니다.

- 귀하는, 이 저작물의 재이용이나 배포의 경우, 이 저작물에 적용된 이용허락조건을 명확하게 나타내어야 합니다.
- 저작권자로부터 별도의 허가를 받으면 이러한 조건들은 적용되지 않습니다.

저작권법에 따른 이용자의 권리는 위의 내용에 의하여 영향을 받지 않습니다.

이것은 [이용허락규약\(Legal Code\)](#)을 이해하기 쉽게 요약한 것입니다.

[Disclaimer](#)

**Study of electron bunching in vacuum devices:
Electron gun, Linear accelerator**

Dongwon Shin

Department of Electrical engineering

Graduate school of UNIST

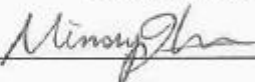
**Study of electron bunching in vacuum devices:
Electron gun, Linear accelerator**

A dissertation
submitted to the Graduate School of UNIST
in partial fulfillment of the
requirements for the degree of
Doctor of Philosophy of Science

Dongwon Shin

6. 12. 2015

Approved by



Advisor

Min Sup Hur

**Study of electron bunching in vacuum devices:
Electron gun, Linear accelerator**

Dongwon Shin

This certifies that the dissertation of Dongwon Shin is approved.

6. 12. 2015



Advisor: Min Sup Hur



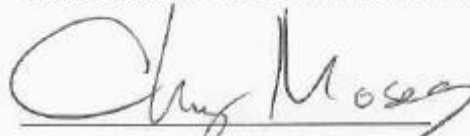
Committee Member : Seok-Gy Jeon



Committee Member : Eunmi Choi



Committee Member : Min-Suk Kwon



Committee Member : Moses Chung

Abstract

Study of electron bunching in vacuum devices: electron gun, linear accelerator

Dongwon Shin

School of Electrical Engineering

Electron bunching is an interesting issue with practical and scientific applications. In this thesis, I will present two topics of electron bunching in vacuum devices: electron gun, linear accelerator. For the electron gun, I will present a theoretical approach of bunching condition in dc-biased ac-driven vacuum devices. There are two different approaches. The one is electron bunching from a DC-biased single surface multipactor. Generation of electron bunch from a dc biased, single surface multipactor was studied theoretically and by PIC simulations. The condition for a spatially narrow bunch was obtained and verified by PIC simulations. This kind of multipactor is proposed to be used as a compact electron gun for various applications, such as linear accelerators. The other one is a theoretical correlation between the periodicity of an electron micro-bunch train and the transit phase of each electrons passing through a vacuum gap in a dc-biased ac-driven diode was derived. The upper frequency limitation by the transit time effect could be explained by abnormal exclusion of a certain range of transit phase analyzed for the first time by our theory. In a particle-in-cell simulation guided by our theory to evade the deficiency, a micro-bunch train with 1.41 picosecond periodicity (0.707 THz) could be obtained from a gap of 50 μm regarded as excessively large owing to severe suffering from the transit time effect.

For the linear accelerator, A 9.3 GHz 6 MeV linear accelerator (LINAC) was analyzed by using three-dimensional (3D) particle-in-cell (PIC) simulations with 3D time-domain electromagnetic simulations. In the 3D PIC simulations, field data of a $\pi/2$ standing wave mode extracted from the 3D time-domain field calculations were injected into a side-coupled LINAC composed of 25 acceleration and 24 coupling cavities. Acceleration of an electron beam of 20 kV, 300 mA in the 3D full LINAC structure was analyzed without spatial or time segmentations, which resulted in maximum energy of 6 MeV and average current of 68.5 mA when 9.3 GHz, 1.6 MW radio frequency (RF) power was assumed. By virtue of in-depth data from the 3D electromagnetic and PIC simulations aided by a one-dimensional (1D) particle code developed by ourselves, the analysis for a full LINAC structure being reported first in this paper, may be informative and useful because experimental reports about an X-band (9.3 GHz) 6 MeV side-coupled LINAC have been rare until now.

Contents

I.	Introduction	1
1.1	Electron bunching in vacuum devices	1
1.2	PIC simulation	5
II.	Electron Bunching From a DC-biased Single Surface Multipactor	7
2.1	Introduction	7
2.2	Furman-Pivi model	8
2.3	Theory	14
2.3.1	Fixed point theory	
2.3.2	Effective longitudinal energy spectrum	
2.4	Conclusion	22
III.	Design of X-band 6MeV side-coupled linear accelerator	23
3.1	Introduction	23
3.1.1	Application of LINAC	
3.1.2	Property of LINAC	
3.1.3	Important parameters of LINAC	
3.1.4	Simulation tools	
3.2	Fundamental Theory and basic study	29
3.2.1	Design flow	
3.2.2	Numerical stabilization	
3.2.3	RF breakdown limit for X-band linear accelerator waveguide	
3.2.4	Energy gain	
3.2.5	Unit cell simulation	
3.2.6	Optimization of linear accelerator	

3.2.7	Electromagnetic simulation for X-band full LINAC cavity waveguide	
3.2.8	3D PIC simulation for X-band full LINAC cavity waveguide	
3.3	Fabrication	46
3.4	Cold test	48
3.5	Conclusion	51
IV.	Generation of an electron micro-bunch train from a dc-biased ac-driven vacuum diode	52
4.1	Introduction	52
4.2	Theory and numerical simulation	54
4.3	Conclusion	60
V.	Summary	61
VI.	References	62

List of Figures

1.1 The typical loop with various techniques for a PIC simulation -----	5
1.2 Leap frog method -----	5
1.3 Movement of particle in mesh -----	6
2.1 (a) The structure of the multipactor. Only the lower plate yields the secondary electrons. The upper plate absorbs the electrons in the simulation. (b) The schematics of the multipactor system. Two parallel plates are driven by the combined dc and ac fields. In a real system the ac field is provided by the radio-frequency wave in a photonic crystal structure. [1] -----	8
2.2 (a) A single electron with energy E_0 and angle θ_0 strikes a surface yielding n secondary electrons with energies $E_1, E_2, E_3, \dots, E_n$ and angles $\theta_1, \theta_2, \theta_3, \dots, \theta_n$. (b) Sketch of the three components of secondary emission processing. -----	8
2.3 Elastic backscattered electron yields for (a) copper and (b) stainless steel from Eq. (2.1). The parameters of the fit are listed in Table 2.1. [2] -----	9
2.4 Rediffused electron yields for (a) copper and (b) stainless steel from Eq. (2.2). The parameters of the fit are listed in Table 2.2. [2] -----	10
2.5 True secondary electron yields for (a) copper and (b) stainless steel from Eq. (2.3). The parameters of the fit are listed in Table 2.3. [2] -----	11
2.6 The emitted-energy spectrum for copper at (a) 10 eV, (b) 30 eV, (c) 300 eV, (d) 500 eV incident energies. -----	12
2.7 The emitted-energy spectrum for stainless steel at (a) 10 eV, (b) 30 eV, (c) 300 eV, (d) 500 eV incident energies. -----	13
2.8 The diagram of the θ distribution which follows $\cos\theta$ and ϕ is uniformly distributed in $0 \sim 2\pi$. -----	16
2.9 Comparison of normalized velocity spectra between MC method and numerical iteration in artificial materials where the parameters are (a) $P_n = 64, \varepsilon_n = 0.01$ (b) $P_n = 4.2, \varepsilon_n = 0.2$. Legend of graph is number density ($/m^3$) of secondary electron at surface. -----	18
2.10 The current diagram of normal direction at the surface of material where the parameter of material are $P_n = 64, \varepsilon_n = 0.01$. We measured the full width of I_{\max} / e . -----	19

2.11 The diagram represented energy spread of secondary electron with angular effect, comparing with simulation results and mapping function, where the parameters are (a) $P_n = 64, \varepsilon_n = 0.01$ (b) $P_n = 4.2, \varepsilon_n = 0.2$ without angular effect and (c) $P_n = 64, \varepsilon_n = 0.01$, (d) $P_n = 4.2, \varepsilon_n = 0.2$ with effective angular effect. -----	20
2.12 Comparison of normalized velocity spectra between MC method and numerical iteration in copper case. -----	21
2.13 PIC simulation of θ area of electron at the copper surface where ϵ is varied. -----	21
3.1 Medical application of LINAC -----	24
3.2 A simplified block diagram of LINAC system -----	24
3.3 Biperiodic standing wave (SW) structures with magnetic side-coupling apertures -----	25
3.4 Effectively normalized electric field at beam path in unit cell structure -----	27
3.5 Stored energy and coupling coefficient in side-coupled LINAC -----	27
3.6 Design flow of X-Band LINAC. The red arrows show critical feed-back processes. -----	29
3.7 (a) Resonance line shape from simulation results of simple cavity and theoretical calculation from Eq. (3.8). The full width at half maximum (FWHM) is equal to the unperturbed frequency ω_0 divided by the Q of the cavity. (b) Cutaway picture of Simple cavity structure. Red arrow is position of RF source in 3D time domain simulation. -----	31
3.8 (a) Cutaway picture of Simple cavity structure with coupler and (b) Electric field magnitude measured from field monitor in 3D CST MWS time domain simulation and theoretical calculation from Eq. (3.9). -----	31
3.9 Vacuum discharge limit for linear accelerator waveguide. -----	32
3.10 Peak electric field decreased by dimensional change of nose part in unit cell structure to avoid vacuum breakdown. -----	33
3. 11 Energy gain of electron beam is calculated by Eq. (3.11), corresponding to total number of unit cells. The required number of cells for 6 MeV acceleration with 70 mA of peak current is 25. -----	35
3.12 (a) Unit cell and full LINAC waveguide with typical values of critical dimension parameters (b) Electric field distributions of 0 mode, $\pi/2$ mode, and π mode in a unit cell extracted from the 3D Eigen mode calculations. -----	36

3.13 (a) Resonant frequencies and (b) frequency deviation, $ f_{N-1} - f_N $, at $\pi/2$ mode in 3D Eigen mode solver while mesh number is swept. The simulation is solved using hexahedral mesh for unit cell structure of X-band LINAC waveguide. -----	37
3.14 (a) Resonant frequencies and (b) frequency deviation, $ f_{N-1} - f_N $, at $\pi/2$ mode in 3D Eigen mode solver while mesh number is swept. The simulation is solved using tetrahedral mesh for unit cell structure of X-band LINAC waveguide. -----	37
3.15 Design parameters of X-band 6 MeV LINAC waveguide where # is cell number -----	38
3.16 Quality factor and shunt impedance of each unit cells in Table 3.3 according to nose height (c) with $r_3 = 0.8$ mm (see Fig. 3.15) -----	40
3.17 Quality factor and shunt impedance of each unit cells in Table 3.3 according to r_3 with $c = 1.2$ mm (see Fig. 3.15) -----	41
3.18 Quality factor and shunt impedance of each unit cells in Table 3.3 according to <i>slot_width</i> with $c = 1.2$ mm and $r_3 = 0.8$ mm (see Fig. 3.15) -----	42
3.19 The electric field distribution obtained by 3D time domain calculations for a LINAC waveguide comprising 25 accelerating and 24 side-coupling cavities is presented. -----	43
3.20 In the upper figure, a stream of electrons is shown on the half cross section of a 9.3 GHz side-coupled LINAC. At the right end of the LINAC, an electron bunch with average energy of 6 MeV is escaping the beam tunnel. The lower figure shows the phase space diagram of electrons. -----	44
3.21 Energy spectrum of electrons calculated by 3D codes and emitted electron density at the end of the LINAC waveguide. -----	45
3.22 Prototype of the X-band 6 MeV side-coupled LINAC waveguide. -----	46
3.23 (a) Bead pull system diagram, (b) Electric field distribution of 3D EM simulation results and measurements with bead pull system -----	48
3.24 S-parameters of X-band full LINAC cavity waveguide reflected by (a) designed value, (b) drawing value, (c) the value measured by 3D coordinate-measuring machine from 3D time domain simulation in CST MWS and (d) VNA measurement value. -----	50
3.25 Comparison of normalized electric distributions between 3D simulation results and experiment by bead pull of X-band 6 MeV full LINAC cavity waveguide -----	50
3.26 Experiment setting for measuring S-parameter and electric field distribution by bead pull of X-band 6 MeV LINAC waveguide -----	51

4.1 Schematics of the dc-biased, ac-driven vacuum diode cavity with a CNT cathode. ----- 54

4.2 (a) Electric field obtained from Eq. (4.1) for various E_d . (b) Emitted beam current from CNT obtained from Fowler-Nordheim formula with $\beta=2.0 \times 10^3$, $\phi_\omega=5.0$ eV, $A=1.56 \times 10^{-6}$ AV²eV, $B = 6.83 \times 10^9$ eV^{-3/2}Vm⁻¹ for various E_d . ----- 55

4.3 (a) Coefficient B in Eq. (7) for $E_d = 0$ for different ϕ 's. (b) Excluded transit phase (the arrowed region). ----- 56

4.4 The map of bunching frequency ω and the final transit phase of electrons for different \bar{E}_d 's. (a) $\bar{E}_d = 0.0$, (b) $\bar{E}_d = -0.2$, (c) $\bar{E}_d = -0.5$, and (d) $\bar{E}_d = -1.0$ ----- 58

4.5 Map of ω vs. $\theta + \phi$, similar to Fig. 4.4, but for extended parameters, (a), (b), (c) with $\bar{E}_d = -0.2$, $\bar{E}_d = -0.5$, and $\bar{E}_d = -0.8$, respectively. (d) the map over the whole range. ----- 59

4.6 Three dimensional PIC simulation of the micro-bunching. The shaded plane marks the upper plane of the cavity. The three-dimensional plot was made via ViSit software [3]. The inset represents the electric current along the bunch train. ----- 60

List of Tables

2.1 Fitting parameters for Eq. (2.1) which is given for copper and stainless steel -----	9
2.2 Fitting parameters for Eq. (2.2) which is given for copper and stainless steel -----	10
2.3 Fitting parameters for Eq. (2.3) which is given for copper and stainless steel -----	11
3.1: Vacuum discharge limit of the research group -----	33
3.2 Given parameters of Eq. (3.11) -----	35
3.3 Important parameters of 3D eigenmode calculation results for unit cells -----	38
3.4 3D eigenmode calculation results for unit cells -----	39
3.5 Variation of important characteristic values by changed dimensional parameters in unit cell cavity (cell No. 5) in Table 3.3. -----	39
3.6 Deviation (D) and error ($\langle \varepsilon \rangle$) in Eq. (3.15) of designed value in draw for fabrication and measured value of cell No.5 in Table 3.3. Number of products (N) is 15. -----	47
3.7 RF characteristics of X-band full LINAC cavity waveguide reflected by (a) designed value, (b) drawing value, (c) the value measured by 3D coordinate-measuring machine from 3D time domain simulation in CST MWS and (d) VNA measurement value -----	49

Chapter 1

Introduction

1.1 Electron bunching in vacuum devices

We studied the influences of wide energy spectrum and emission angle of secondary electrons on electron bunching from a dc-biased single surface multipactor. In our previous study of the same system, an ideally narrow energy spread of secondary electrons without emission angle was used in the analysis of the electron trajectory [1,4]. In this paper, we investigated the cases with realistic energy spectrum, which is featured by a wide energy spread and significant emission angle. To theoretically approach the matter of emission angle, we employed a concept of effective longitudinal velocity distribution. The theoretical results are verified by PIC (Particle-In-Cell) simulations. We also studied the electron bunching from a copper by PIC simulations, where we observed stable electron bunches with bunch width of approximately $80\mu\text{m}$.

The multipactor discharge is prevalent in many rf devices [5–10]. Like other discharge processes, the multipactor is also associated with electron avalanche: some free initial electrons inside the device are accelerated by rf field to hit the material surface, yielding more secondary electrons. Then the emitted secondary electrons hit again after several period of the rf and make even more secondary electrons. As this procedure is periodically repeated, the number of free electrons in vacuum increases rapidly. This event, which occurs in most rf devices, is usually undesirable, since it can damage to the window of the rf device [11–13] or change the conditions of device operation [11]. Sometimes the multipactor leads even to vacuum breakdown [12,13]. Despite these undesirable features, there is a stream of utilizing it for a high intensity electron beam generation [14,15]. For example, there can appear electron bunches, which have narrow sizes and high intensities, if some inherent resonance conditions are satisfied [1,4,15]. One of the multipactor discharge structures suitable for that purpose, i.e. the bunch generator, is the dc-biased single surface multipactor [1].

In our previous works on this system, the fixed point theory with space charge effect neglected has been studied [1,4]. From the theory and simulations, it was found that narrow bunches of electrons can be generated stably if some stability conditions are satisfied. Such conditions were derived analytically from the quadratic mapping of a given phase deviation to the next cycle phase deviation [1,4]. And from by same mapping, the effects of a small, square-shaped energy spread in the secondary emission energy have been investigated [4].

In this paper, we extend our previous work to include more realistic effects. First of all, we investigated the cases with realistically wide spectrum of emission energy of the secondary electrons. The materials we first considered here are some artificial materials with broader spectra than before

and then we studied the case with a copper eventually. For analysis, we used the previously developed quadratic mapping [4] and PIC simulations. Second, we considered the effects of emission angle of secondary electrons. For the implementation of the angle effect to our previous one-dimensional theory, we employed the concept of the ‘effective’ secondary emission energy spectrum in normal direction to the surface. We compared the mapping theory with such ‘effective’ spectrum with PIC simulations, from which a good agreement was obtained.

In chapter 2, The paper is organized as follows: first previous work on the fixed point theory is reviewed. And we present effective longitudinal energy spectrum by material property and angular effect of true secondary electron along with PIC simulation.

LINAC has been widely applied for medical radiotherapy [16–20], non-destructive imaging [21–23] and various industrial uses [24–26]. In such applications, the electron beam energy at the end of a LINAC waveguide is typically less than 10 MeV and a S-band (~3 GHz) LINAC waveguide is employed in most modern radiotherapy machines. For medical application, majority of radiotherapy machines are composed of several isocentric devices [27–29] including a LINAC waveguide and those are packed in an accurately motion controlled gantry moving around an isocenter on a patient’s body. From an engineering point of view to make the gantry system easy to design and manufacture, minimizing the LINAC waveguide is crucial because all of the medical LINACs as well as most of LINACs for industrial applications should be surrounded by a massive radiation shield made of lead. Therefore, an all-in-one LINAC waveguide structure, an assembly of a buncher section and an acceleration section connected with a simple thermionic electron gun, has been adopted. Recently, development of compact LINACs such as C-band (~5.7 GHz) [17,20,28,30–33] and X-band LINACs with a side-coupled cavity waveguide [21] or an axially coupled cavity waveguide [24,34,35] have been the subject of great interest because of their merits as proven by the Cyberknife. In contrast with the machines employing a S-band medical LINAC, the Cyberknife [36] has the most compact medical LINAC, a X-band (9.3 GHz) LINAC, which is connected to a robotic arm. By virtue of its compactness and lightness, the Cyberknife has a high degree of motion freedom owing to such unique configuration employing a robotic arm.

To achieve the same energy of electrons in an X-band LINAC, three times as many coupled cavities are required as for the S-band LINAC. Therefore the design technology for X-band LINACs needs higher accuracy compared with S-band LINACs [4,11,22,23]. Moreover, to design an advanced medical LINAC integrated with a functional apparatus such as an MRI delivering non-radiative image guiding for radiotherapy, accurate 3D LINAC design technologies dealing with multi-physics are necessary because the analysis of electron beam acceleration within non-uniform magnetic fields is an important issue in MR-LINAC [37]. One well-known code to calculate the electromagnetic field in the cavities of a LINAC waveguide is the SUPERFISH [33,35,39], which has been mainly applied to

axially symmetric structures. To analyze non-symmetric structures like the side-coupled cavity waveguide, recent codes such as COMSOL [37], CST [20,40], and MAGIC [26] have been used. In this paper, we report a LINAC design process mainly depending on 3D electromagnetic and PIC simulations. CST MWS and PS [40] were used for the 3D computations. A 1D particle code was developed by our group to get a quick estimation prior to the time-consuming 3D computations. Based on the computational design, a side-coupled 9.3 GHz 6 MeV LINAC waveguide was fabricated and brazed. The bead pull test without performing mechanical tuning of any cavity was carried out to measure the electric field distribution suspending at the center line of cavity waveguide. The comparison between the results from experiment and computer simulation showed an error of below 20%. As far as we know, the error is acceptably small for an X-band 6 MeV side-coupled cavity waveguide because the field data are compared without any mechanical tuning of the cavity waveguide.

For the past few years, the generation of an electron micro-bunch train with sub-picosecond periodicity has been a subject of great interest, owing to its feasibility of being used for coherent terahertz (THz) radiation [41,42]. One popular method to produce such short-period micro-bunches is using a photocathode with carefully manipulated laser pulses [43–45]. Activating spatial beam-wave interaction [41,46] or creating a virtual cathode in a diode [47,48] are also interesting ways to generate tunable micro-bunches.

The methods described above usually demand big acceleration facilities or fine control of laser systems, whereas the electron bunch train can also be generated simply by gating the electric field between the cathode and grid in a vacuum diode cavity (klystrode) [49–51], which has been used in the microwave regime historically. Though lots of efforts have been devoted to extending the operation frequency of this device to tens of gigahertz (GHz) or sub-THz, no success has been achieved in breaking the upper barrier at a few GHz, due to the inherent upper frequency limitation given by the well-known *transit time effect*: as the operation frequency increases, some electrons return to the cathode surface or are decelerated by encountering the reversed electric field, which eventually blurs the bunching and weakens the intensity of the bunches.

Conventionally it has been believed that the transit time effect can be suppressed in a reduced gap, which ensures escaping of electrons by extricating them from the reversed field. In such a case, electrons may escape the gap before facing the reversed electric field. Reduction of the gap distance down to 1 μm demonstrated by the field emission arrays (FEAs) [52–55] seemed to be the best solution to counteract the transit time effect. However, the modulation frequency of electron bunching has been strictly limited under tens of GHz, due to the large capacitance originating from short gap distances [43]. Though CNT (carbon nano tube)-based cold cathodes [56–58] enable significant reduction of the gap distance, the shortest periodicity of the electron bunch train ever demonstrated

experimentally from a CNT cathode up to now is merely above 1.5 GHz [56], seemingly due to the transit time effect. While the transit time effect in vacuum diodes is regarded as a crucial factor to prohibit increasing the modulation frequency, the physical understanding of this phenomenon still remains at just an intuitive level or phenomenological from the experimental results.

In this paper, for the first time as far as we know, a fully quantitative, theoretical understanding of the transit time effect on the modulation frequency in a vacuum diode is provided, along with physical conditions to break that limit. Using the concept of excluded transit phase (ETP), we quantitatively explain why the upper frequency barrier had resided at around just a few GHz in the previous research [42,49–56,59]. ETP, which is one of the interesting phenomena we discovered theoretically in this work, means that a certain range of the transit phase can be wholly excluded, so that any micro-bunches emitted with ETP collapse before they reach the anode grid. Additionally, we reveal that the normally-believed demand for reduced gap distance to relax the transit time effect is a misguided constraint, by showing that spatial separation between bunches traversing a wide gap can be well preserved as long as the excluded transit phase is sufficiently suppressed by means of dc bias. Subsequently, from a three-dimensional particle-in-cell simulation, a train of well-separated micro-bunches with 1.41 picosecond periodicity (0.707 THz) could be obtained, perfectly matching the theoretical prediction, even for 50 μm -wide gap spacing, where a significant transit time effect had been expected.

1.2 PIC simulation

Theoretical studies on electron bunching in vacuum devices involve Maxwell’s equation and the force equation like the Lorentz force. The numerical calculation offers the solution and reduces the consumption of energy, time and efforts. Though plasma simulation methods have several classes such as kinetic, fluid, and hybrid method, I will treat PIC code as a kinetic method. A PIC code is composed of the field solver, applying the field value to each particle, the particle movement and the current calculation, which form one calculation loop [60]. Various techniques for the calculations can be imported in a code like a surface reaction.

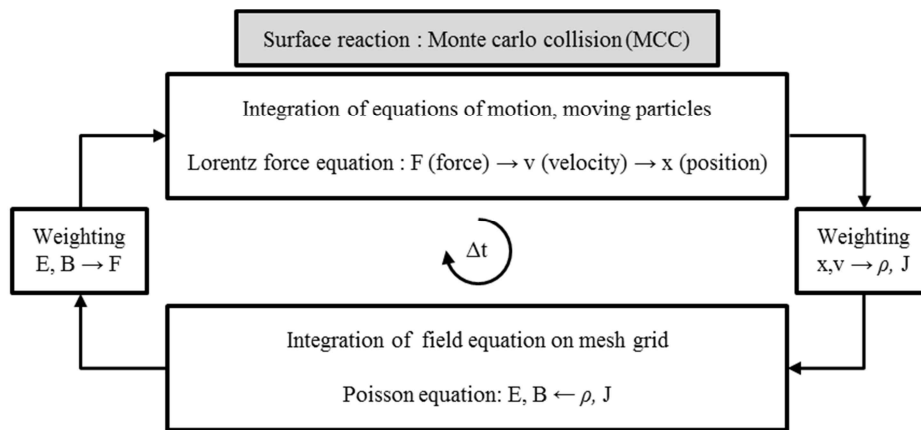


Figure 1.1: The typical loop with various techniques for a PIC simulation

$$m_i \frac{d\vec{v}_i}{dt} = q_i \vec{E}_i + q_i \vec{v}_i \times \vec{B}_i + \text{MCC collision} \quad (1.1)$$

Monte Carlo methods are a broad class of computational algorithms that rely on repeated random sampling to obtain numerical results. They are often used in physical and mathematical problems and are most useful when it is difficult or impossible to use other mathematical methods. Monte Carlo methods are mainly used in three distinct problem classes: optimization, numerical integration, and generating draws from a probability distribution.

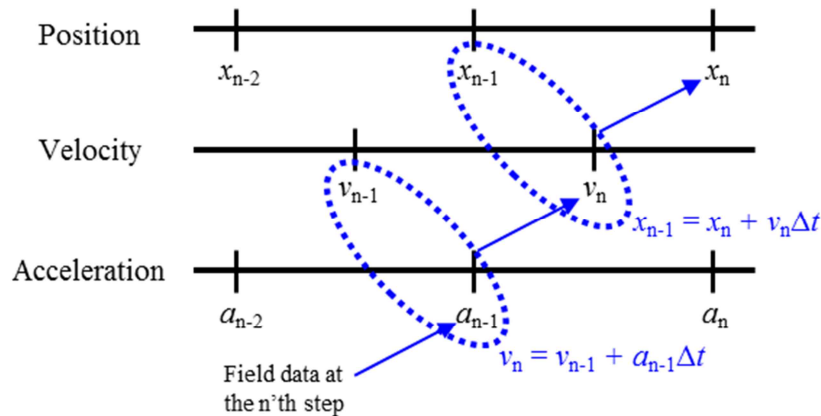


Figure 1.2: Leap frog method

Velocity and position integration leap over each other, being displaced by half a time step. particle positions exist at the integral time steps, while velocity exists at the half times.

The Lorentz force equation is defined as:

$$a_t = \frac{u_{t+\Delta t/2} - u_{t-\Delta t/2}}{\gamma \Delta t} = \frac{q}{m} \left[E_t + \frac{u_{t+\Delta t/2} + u_{t-\Delta t/2}}{2\gamma} \times B_t \right] \quad (1.2)$$

where $(u_{t+\Delta t/2} + u_{t-\Delta t/2})/2\gamma$ is averaged velocity (ref. Buneman, J. Comp. Phys. 1967.)

The averaged velocity is divided by relativistic factor.

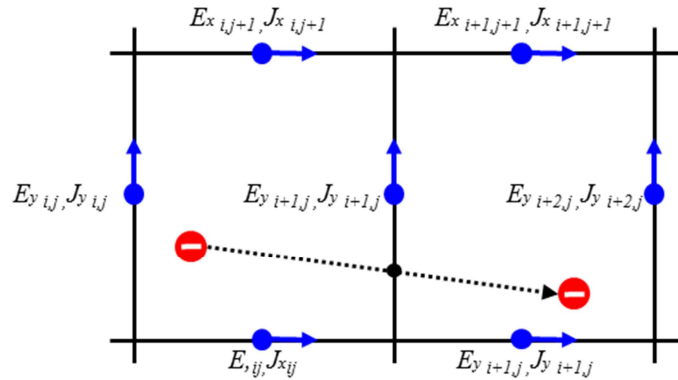


Figure 1.3 Movement of particle in mesh

$$J_{x,i,j} = \frac{q\Delta W_x(1 - \bar{W}_y)}{\Delta y \Delta t}, J_{x,i,j+1} = \frac{q\Delta W_x(\bar{W}_y)}{\Delta y \Delta t} \quad (1.3)$$

According to position and velocity of particle, the value of current at mesh point is determined by area in two dimensions. The value is determined by volume in three dimensions. Summation of each area or volume is one.

Chapter 2

Electron Bunching From a DC-biased Single Surface Multipactor

2.1 Introduction

The multipactor discharge is prevalent in many rf devices [5–10]. Like other discharge processes, the multipactor is also associated with electron avalanche : some free initial electrons inside the device are accelerated by rf field to hit the material surface, yielding more secondary electrons. Then the emitted secondary electrons hit again after several period of the rf and make even more secondary electrons. As this procedure is periodically repeated, the number of free electrons in vacuum increases rapidly. This event, which occurs in most rf devices, is usually undesirable, since it can damage to the window of the rf device [11–13] or change the conditions of device operation [11]. Sometimes the multipactor leads even to vacuum breakdown [12,13]. Despite these undesirable features, there is a stream of utilizing it for a high intensity electron beam generation [14,15]. For example, there can appear electron bunches, which have narrow sizes and high intensities, if some inherent resonance conditions are satisfied [1,4,15]. One of the multipactor discharge structures suitable for that purpose, i.e. the bunch generator, is the dc-biased single surface multipactor [1].

In our previous works on this system, the fixed point theory with space charge effect neglected has been studied [1,4]. From the theory and simulations, it was found that narrow bunches of electrons can be generated stably if some stability conditions are satisfied. Such conditions were derived analytically from the quadratic mapping of a given phase deviation to the next cycle phase deviation [1,4]. And from by same mapping, the effects of a small, square-shaped energy spread in the secondary emission energy have been investigated [4].

In this paper, we extend our previous work to include more realistic effects. First of all, we investigated the cases with realistically wide spectrum of emission energy of the secondary electrons. The materials we first considered here are some artificial materials with broader spectra than before and then we studied the case with a copper eventually. For analysis, we used the previously developed quadratic mapping [4] and PIC simulations. Second, we considered the effects of emission angle of secondary electrons. For the implementation of the angle effect to our previous one-dimensional theory, we employed the concept of the ‘effective’ secondary emission energy spectrum in normal direction to the surface. We compared the mapping theory with such ‘effective’ spectrum with PIC simulations, from which a good agreement was obtained. (Fig. 2.1)

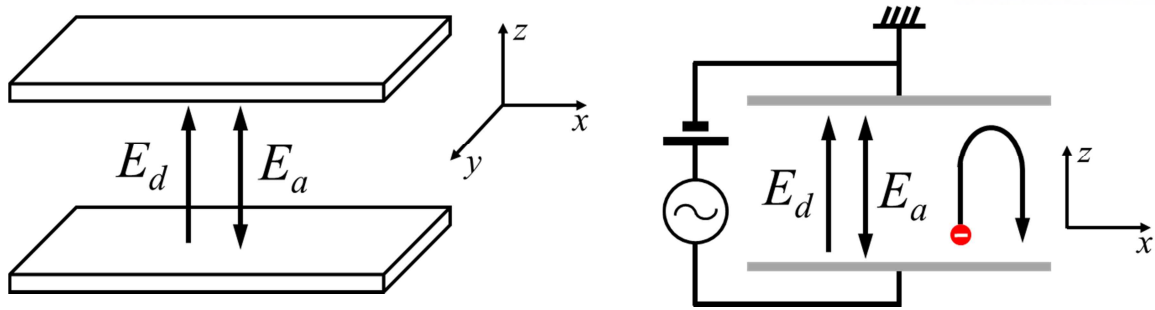


Figure 2.1: (a) The structure of the multipactor. Only the lower plate yields the secondary electrons. The upper plate absorbs the electrons in the simulation. (b) The schematics of the multipactor system. Two parallel plates are driven by the combined dc and ac fields. In a real system the ac field is provided by the radio-frequency wave in a photonic crystal structure. [1]

2.2 Furman-Pivi model

Furman and Pivi's model provides analytic form about reflecting process of incident electron and secondary electron emission. Since models for secondary emission processing have researched, the Furman-Pivi model is appropriated to use the PIC code. The model is based on a broad phenomenological fit to data for the secondary emission yield (SEY) and the emitted-energy spectrum (Fig. 2.2 (a)). In this paper, two particular data sets, one for copper and the other one for stainless steel, is described by applying Furman-Pivi model [2].

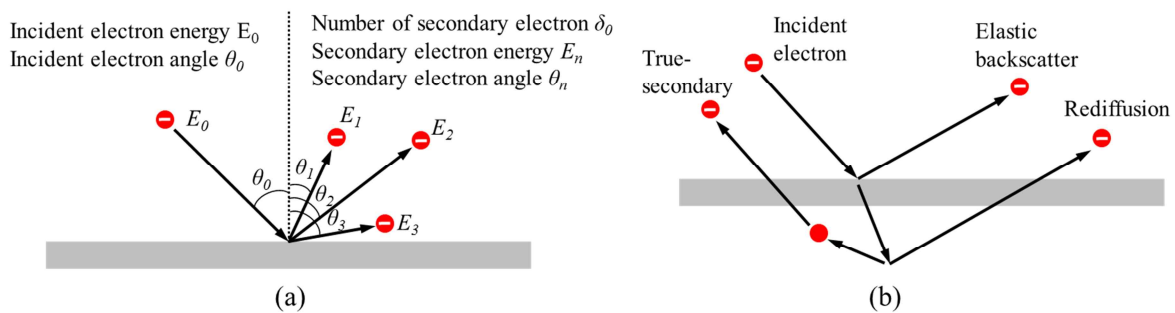


Figure 2.2: (a) A single electron with energy E_0 and angle θ_0 strikes a surface yielding n secondary electrons with energies $E_1, E_2, E_3, \dots, E_n$ and angles $\theta_1, \theta_2, \theta_3, \dots, \theta_n$. (b) Sketch of the three components of secondary emission processing.

The conventional picture of secondary emission, which is based on various reviews of the subject, can be summarized as the three components of the SEY (secondary electron yield) in Fig 2.2 (b). When electrons strike the surface, a certain electrons are backscattered elastically while the rest penetrates into the material. Some of these electrons scatter from one or more atoms inside the material and are reflected back out. The rest of the electrons interact in a more complicated way with

the material and yield.

The yield (δ_e) for elastic backscattered electrons have the form:

$$\delta_e = P_{0,e} + (\hat{P}_{0,e} - P_{0,e})e^{-(|E_0 - \hat{E}_e|/W)^p / p}, \quad (2.1)$$

where $P_{0,e}, \hat{P}_{0,e}, \hat{E}_e, W, p$ is fitting parameters which is given for copper and stainless steel in Table 2.1.

Table 2.1 Fitting parameters for Eq. (2.1) which is given for copper and stainless steel

Given parameters	Copper	Stainless steel
$P_{0,e}$	0.02	0.07
$\hat{P}_{0,e}$	0.496	0.5
\hat{E}_e	0	0
W	60.86	100
p	1	0.9

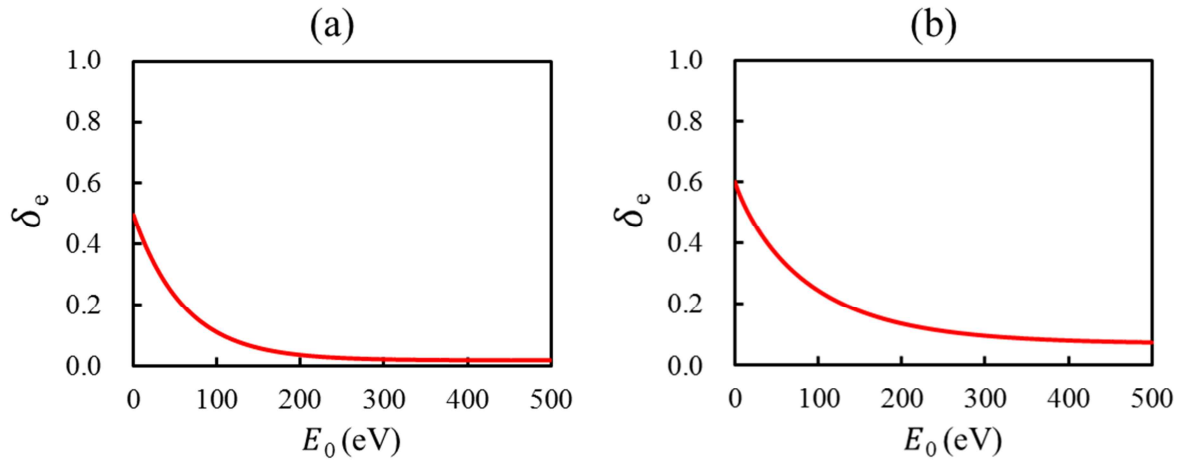


Figure 2.3: Elastic backscattered electron yields for (a) copper and (b) stainless steel from Eq. (2.1).

The parameters of the fit are listed in Table 2.1. [2]

The yield (δ_r) for rediffused electrons have the form:

$$\delta_r = P_{0,r}(1 - e^{-(E_0/E_r)^r}), \quad (2.2)$$

where $P_{0,r}, E_r, r$ is fitting parameters given for materials which is given for copper and stainless steel in Table 2.1.

Table 2.2 Fitting parameters for Eq. (2.2) which is given for copper and stainless steel

Given parameters	Copper	Stainless steel
$P_{0,r}$	0.02	0.07
E_r	0.496	0.5
r	0	0

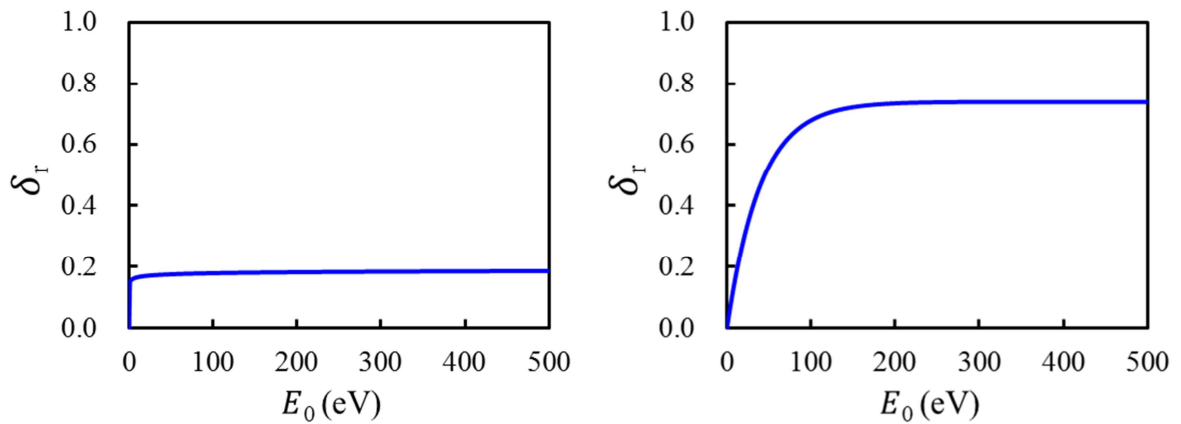


Fig. 2.4: Rediffused electron yields for (a) copper and (b) stainless steel from Eq. (2.2).

The parameters of the fit are listed in Table 2.2. [2]

The yield (δ_{ts}) for rediffused electrons have the form:

$$\delta_{ts} = \hat{\delta} \frac{sx}{s-1+x^s}, \quad x = \frac{E_0}{\hat{E}}, \quad (2.3)$$

where $\hat{\delta}, s, \hat{E}$ is fitting parameters given for materials.

Table 2.3 Fitting parameters for Eq. (2.3) which is given for copper and stainless steel

Given parameters	Copper	Stainless steel
$\hat{\delta}$	1.8848	1.22
s	1.54	1.813
\hat{E}	276.8	310

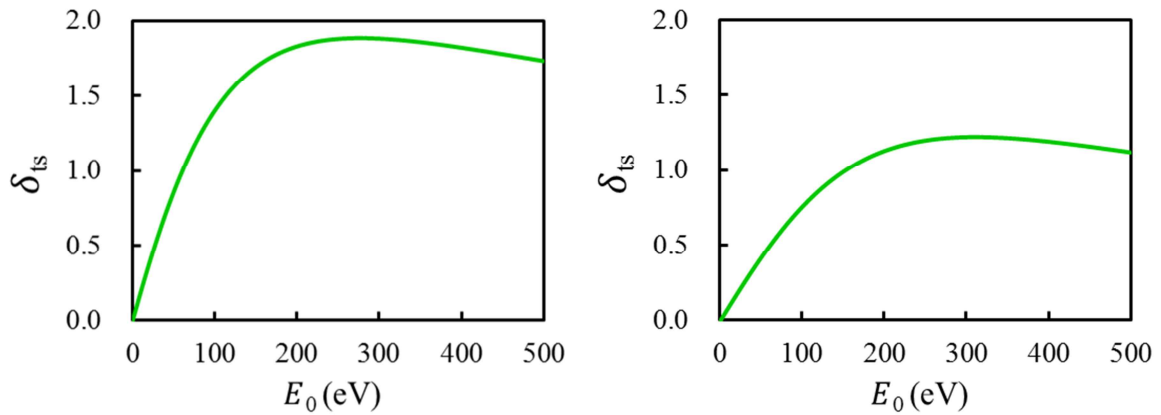


Fig. 2.5: True secondary electron yields for (a) copper and (b) stainless steel from Eq. (2.3).

The parameters of the fit are listed in Table 2.3. [2]

For the energy probability functions of three components in [2] have forms:

$$f_e(E) = \delta_e \frac{2e^{-(E-E_0)^2/2\delta_e^2}}{\sqrt{2\pi}\sigma_e \operatorname{erf}(E_0/\sqrt{2}\sigma_e)} \quad (2.4)$$

$$f_r(E) = \delta_r \frac{(q+1)E^q}{E_0^{q+1}} \quad (2.5)$$

$$f_{n,ts}(E) = F_n E^{P_n-1} e^{-E/\varepsilon_n} \quad (2.6)$$

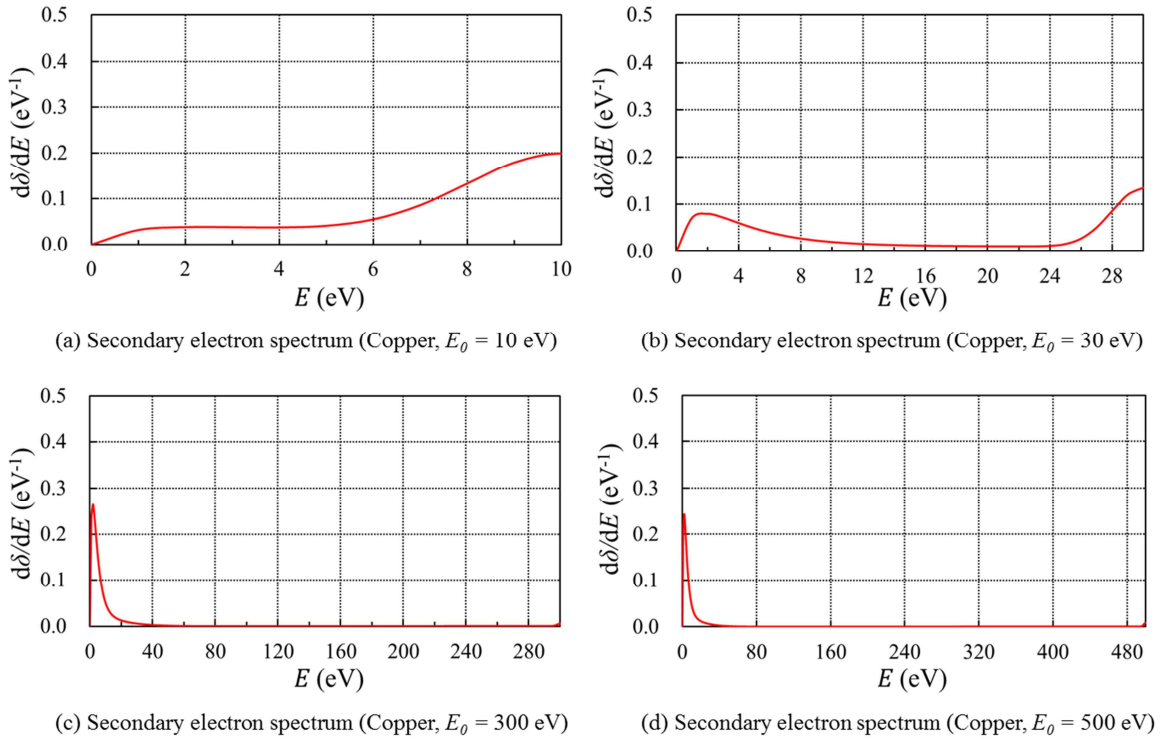
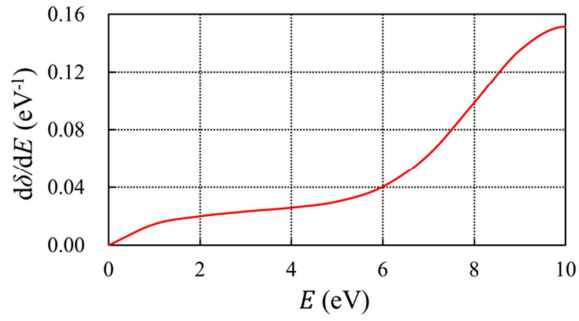
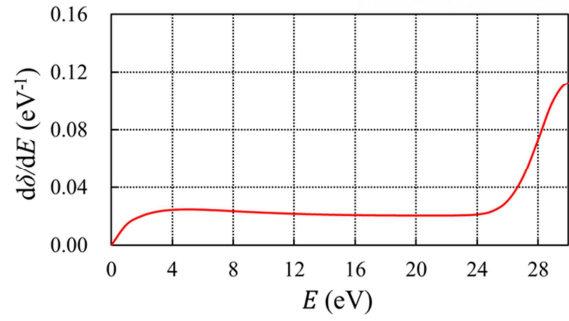


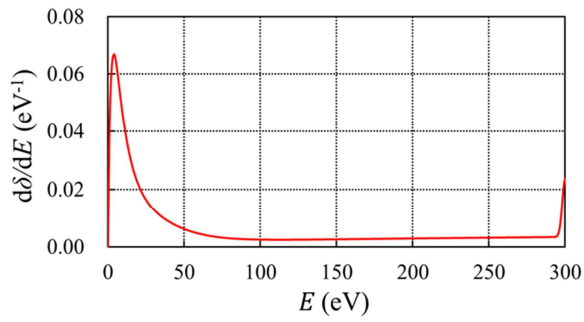
Fig. 2.6: The emitted-energy spectrum for copper at (a) 10 eV, (b) 30 eV, (c) 300 eV, (d) 500 eV incident energies.



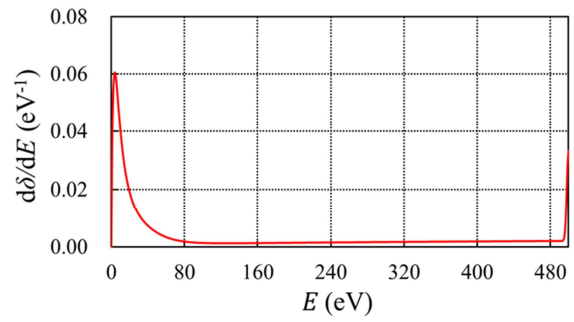
(a) Secondary electron spectrum (Steel, $E_0 = 10$ eV)



(b) Secondary electron spectrum (Steel, $E_0 = 30$ eV)



(c) Secondary electron spectrum (Steel, $E_0 = 295$ eV)



(d) Secondary electron spectrum (Steel, $E_0 = 500$ eV)

Fig. 2.7: The emitted-energy spectrum for stainless steel at (a) 10 eV, (b) 30 eV, (c) 300 eV, (d) 500 eV incident energies.

2.3 Theory

2.3.1 Fixed point theory

In this section, we review the fixed point equation to calculate analytically the electron trajectories for bunching and its stability condition. If the electron trajectory in the structure is assumed to depend only on the external dc and ac field without space charge effect, the single electron equation of motion is given by

$$\frac{d^2 z}{dt^2} = -\frac{e}{m} E_d - \frac{e}{m} E_a \sin(\omega t + \theta_0), \quad (2.7)$$

where E_d and E_a are amplitudes of dc and ac fields. E_d has to be large enough to yield secondary electrons. And also E_a must be adequately larger than E_d to prevent premature impact. The integration of Eq. (2.7) yields the trajectory equation of the secondary electron.

$$z(t) = \left(v_0 - \frac{eE_a}{m\omega} \cos(\theta_0) \right) t - \frac{eE_d}{2m} t^2 + \frac{eE_a}{m\omega^2} [\sin(\omega t + \theta_0) - \sin(\theta_0)], \quad (2.8)$$

where $z(t=0)=0$. When the electron returns to the emission plate after the n'th cycle of ac field, the secondary electron should start with the same initial velocity v_0 . So with $z=0$ at $t=2\pi n/\omega$ in Eq. (2.8), the resonance equation is given by

$$\cos \theta_0 = \nu - n\pi\varepsilon, \quad (2.9)$$

where $\varepsilon = E_d/E_a$, $\nu = m\omega/eE_a v_0$. Here ε represents the ratio of ac and dc field, and ν the normalized emission velocity of secondary electrons.

For a resonant electron to tolerate any perturbed deviation from its resonant trajectory, it should be in a certain range of stability condition. To find the stability condition of the fixed point, we derived a quadratic function, which mapped the deviation $\Delta_k = \theta_k - \theta_0$ at the k'th cycle to Δ_{k+1} at the next cycle.

If it takes τ_k for an electron to finish its cycle $\Delta_{k+1} = \theta_{k+1} - \theta_0 = \theta_k + \tau(\theta_k) - \theta_0 - \tau(\theta_0)$, where $\tau(\theta_0) = 2n\pi$ and τ is the time for the electron to return to the emission plate. Here θ_k is the initial phase at the k'th cycle, and θ_0 is the fixed point from Eq. (2.8). By Taylor expansion up to the second order of Δ_k , we obtain

$$\frac{\Delta_{k+1}}{\Delta_k} = 1 + \frac{\tau(\theta_k) - \tau(\theta_0)}{\theta_k - \theta_0} \approx 1 + \left. \frac{\partial \tau}{\partial \theta} \right|_{\theta_0} + \frac{\Delta_k}{2} \left. \frac{\partial^2 \tau}{\partial \theta^2} \right|_{\theta_0}. \quad (2.10)$$

From $z(\tau/\omega) = 0$, we could obtain $\partial_\theta \tau$ and $\partial_\theta^2 \tau$.

$$\tau'_0 = -\frac{2n\pi \sin \theta_0}{v - 2n\pi\varepsilon} = \frac{2n\pi \sqrt{1 - (v - n\pi\varepsilon^2)}}{v - 2n\pi\varepsilon}, \quad (2.11)$$

$$\tau''_0 = \frac{2n\pi}{(v - 2n\pi\varepsilon)^3} \left[2n\pi \left(\varepsilon - \sqrt{1 - (v - n\pi\varepsilon)^2} \right)^3 - (v - n\pi\varepsilon) (v^2 - 2n\pi\varepsilon v + 2n^2\pi^2\varepsilon^2) \right]. \quad (2.12)$$

Equation (2.10) can be simply written by a quadratic function as

$$\Delta_{k+1} = f(\Delta_k) = \Delta_k (b + a\Delta_k), \quad (2.13)$$

where $a = \tau''_0/2$, $b = 1 + \tau'_0$.

From a standard quadratic mapping analysis, the stability condition for the fixed point θ_0 can be set as $|b| < 1$. If the stability condition is satisfied, the electron phase will converge to the fixed point as iteration goes on, even though there exists some perturbation in its trajectory.

We also considered the energy spread of the secondary electrons. To do that, the mapping function was modified as follows.

$$\theta_{k+1} = \theta_k + \tau(v_k, \theta_k) - \tau(v_0, \theta_0), \quad (2.14)$$

where $v_k = v_0 + \delta v_k$. As we use the Taylor expansion on Eq. (2.14) up to the second order, we approximately obtain

$$\theta_{k+1} = \theta_k + \Delta_k \tau'_0 + \delta v_k \partial_v \tau_0 + \frac{1}{2} \Delta_k^2 \tau''_0 + \Delta_k \delta v_k \partial_v \tau'_0 + \frac{1}{2} \delta v_k^2 \partial_v^2 \tau_0, \quad (2.15)$$

where $\Delta_k = \theta_k - \theta_0$. For the convenience in analysis, we represent Eq. (2.15) as follows.

$$g(x) = x(\hat{b} + ax) + s, \quad (2.16)$$

where $\hat{b} = b + \delta v_k \partial_v \tau'_0$ and $s = \delta v_k \partial_v \tau_0 + \frac{1}{2} \delta v_k^2 \partial_v^2 \tau_0$, $a = \tau''_0/2$, $b = 1 + \tau'_0$, $g(x) = \Delta_{k+1}$, $x = \Delta_k$. In our previous work we studied the case, where δv_k is small compared to the peak value of v_0 . Equation (2.16) was numerically calculated and calculation of mapping was verified by PIC simulation.

2.3.2 Effective longitudinal energy spectrum

In this section, we study the characteristics of the electron bunches, when more realistic features of secondary emission are included. Here the realistic features can be described by two properties, which were not counted in our previous works [1,4]: one is the much wider energy spectrum of the secondary electrons and the other is the non-zero emission angle. The energy spread effect is already included in the mapping theory via the ‘s’-term in Eq. (2.16). Previously we studied a very narrow, square-shaped emission energy spectrum [4], where $\Delta v/v < 0.05 \sim 0.15$. Here we apply the same mapping theory to the case with a broader, Gaussian-like realistic energy spectrum with $\Delta v/v < 0.1 \sim 0.5$. Furthermore, to account for the emission angle effects of the secondary electrons by the one-dimensional mapping theory, we derived the ‘effective’ emission spectrum of longitudinal velocity, which was implemented to the energy spread term in the mapping theory. The iteration results of the mapping were compared with PIC simulations. We also studied the electron bunching from a copper plate, which has even a wider emission energy spectrum. For such a very wide energy spectrum, our mapping theory is not valid any more, since Eq. (2.16) has derived from the Taylor expansion for small Δ_k only. In that case, we performed just the PIC simulations to obtain the electron bunching size in the phase space and current profile.

For the realistic energy spectrum and emission angle of the secondary electrons, we used the analytic fitting formulae in Furmann and Pivi’s paper [61]. In reference [61], the authors described the energy distribution of secondary electrons from the surface of material, for a given energy and incident angle of a primary electron : the emission energy distribution of true secondary electrons is determined by $f_n(E) = F_n E^{P_n-1} e^{-E/\varepsilon_n}$, where F_n is a normalizing factor, which depends on fitting parameters of material P_n, ε_n . This is for the true secondary emission, which dominates the energy spectrum more than other secondary emission mechanisms such as backscatter or rediffused [61].

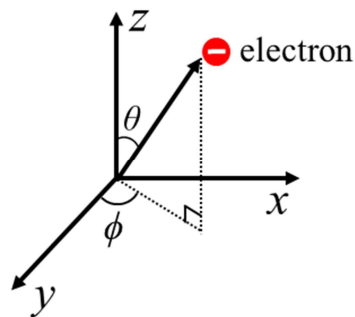


Figure 2.8: The diagram of the θ distribution which follows $\cos\theta$ and ϕ is uniformly distributed in $0 \sim 2\pi$.

As is implied from our one dimensional analysis, distribution of v_z (longitudinal velocity) is important in determining the trajectories of electrons and bunching. At this point we use velocity distribution instead of energy. The emission angle follows the $\cos\theta$ distribution, and azimuthal angle is uniformly distributed in $0 \sim 2\pi$ [61] as in Fig. 2.8. The parallel component of the velocity does not influence much the bunching as long as the transverse dimension of the system is large enough compared to the transverse deviation of electrons for one cycle (This point was verified by PIC simulations). To obtain v_z -distribution with emission angle spread considered, we start from

$$E = \frac{1}{2} \frac{eE_a^2}{m\omega} \frac{v_z^2}{\cos^2\theta}, \quad (2.17)$$

which are from $E[eV] = \frac{1}{2e}mv^2[eV]$, $v = \frac{eE_a}{m\omega}v$ and $v = \frac{v_z}{\cos\theta}$. Emission angle and energy variation of the probability distribution can be expressed by: $dP(E, \theta) = A f_n(E) \cos\theta d\theta dE$, where $f_n(E) = F_n E^{P_n-1} e^{-E/\varepsilon_n}$ and A is a normalizing constant. Then from Eq. (2.17), we obtain

$$dP(v_z, \theta) = \frac{A' v_z f_n'(v_z, \theta)}{\cos\theta} dv_z d\theta \quad (2.18)$$

By averaging over ε we obtain

$$dP(v_z) \approx \langle dP(v_z, \theta) \rangle_\theta dv_z = F(v_z) dv_z, \quad (2.19)$$

where $F(v_z) = \int_0^{\frac{\pi}{2}} \frac{A' f_n'(v_z, \theta) v_z}{\cos\theta} d\theta$. Here $F(v_z)$ actually means the probability distribution of speed

in z-direction considering the effect of the emission angle.

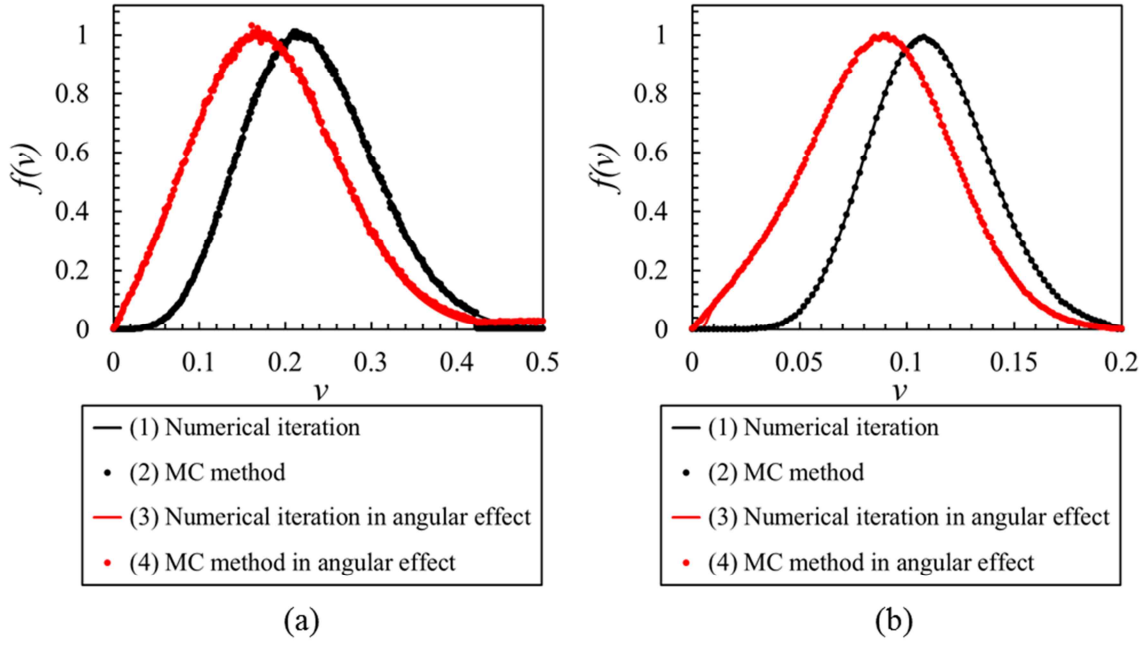


Figure 2.9: Comparison of normalized velocity spectra between MC method and numerical iteration in artificial materials where the parameters are (a) $P_n = 64, \varepsilon_n = 0.01$ (b) $P_n = 4.2, \varepsilon_n = 0.2$. Legend of graph is number density ($/\text{m}^3$) of secondary electron at surface.

The numerical integration of $F(\nu_z)$ can be compared with velocity distribution obtained from Monte-Carlo (MC) method. In MC method, we used the accept-reject method, where two random numbers are used. The procedures are that the first random number R_1 is chosen from the range $[0, E_{\max}]$, where E_{\max} is the maximum true secondary electron energy. The first random number is used to calculate $f(R_1) = A'E^{P-1}e^{E/\varepsilon}$. Then the second random number R_2 is uniformly generated between $0 \sim 1$. The random number generation is repeated until we obtain $R_2 < f(R_1)$ then R_1 is converted to the normalized velocity $\nu = 2\omega\sqrt{R_1}/E_a$. We used 10^5 test electrons to get ν_z distribution. We compared the effective longitudinal velocity distributions calculated from Eq. (2.19) and from the MC calculation in Fig. 2.9. The material parameters were ($P_n = 65, \varepsilon_n = 0.01$) and ($P_n = 4.2, \varepsilon_n = 0.2$) which correspond to $\nu = 0.1 \pm 0.01$ and $\nu = 0.1 \pm 0.05$, respectively. These energy spreads are much wider than the cases in Ref. [4]. From Fig. 2.9, it looks like that by the emission angle of secondary electrons, their effective longitudinal velocity distribution is generally broadened and the peak position is shifted to the lower side. And in the case (a) of Fig 2.9, which has narrower spectrum than Fig. 2.9 (b), the peak position is shifted less : the shifted intervals of (a) and (b) are $\Delta\nu = 0.0044$ and 0.0186 . On the other hand the spectral width of ν_z in case (a) is much wider than case (b). Note that numerical iteration and MC method agree well with each other.

With these modified longitudinal velocity distribution of the secondary electrons, we iterated Eq. (11) to obtain phase diagrams. We also performed PIC simulations for comparisons. For the PIC simulations the empirical formulae in Ref [61] were implemented to the secondary electron routine of the code. The secondary emission routine allows a full energy spectrum of the secondary emission, which is composed of back scattering, rediffusion and true secondary electron emission [62]. The width of material surface was 200 μm in transverse direction, and the longitudinal length of the system was 200 μm . We fixed the frequency and ac field amplitude at 35GHz and 5.941 V/ μm , respectively, and the dc field was varied.

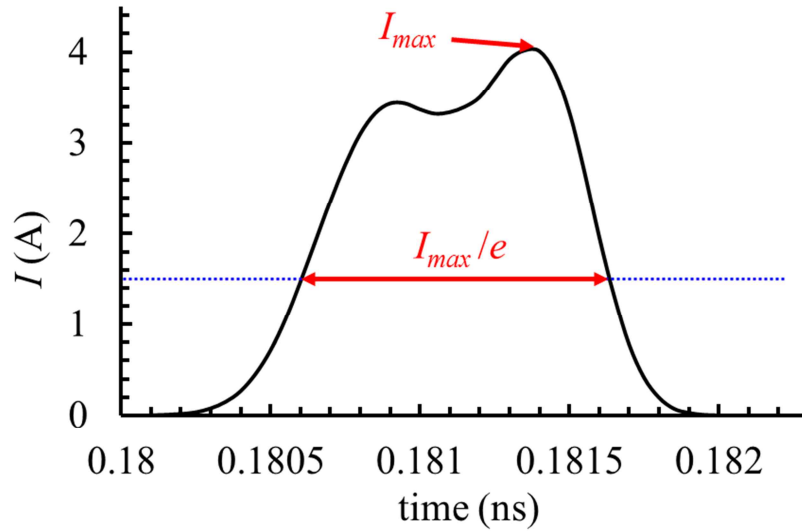


Figure 2.10: The current diagram of normal direction at the surface of material where the parameter of material are $P_n = 64$, $\varepsilon_n = 0.01$. We measured the full width of I_{\max}/e .

To extract the phase information of the electron bunches from the PIC simulations, we measured the full width at I_{\max}/e electric of the current through the emission plate as in Figure 2.10, and converted it to the phase following the procedure in Ref. [4]. Electrons phase spread obtained in this way were compared with the results from mapping Eq. (2.16). Note that the width of the phase spread is proportional to the longitudinal size of the bunch. Figure 2.11 shows comparison of phase spread from the simulations and Eq. (2.16). Red error bars actually represent the phase range measured from simulations. The yellow~blue colors mean density of numbers how frequently the phase θ_k hits on any specific value during the iteration of Eq. (2.16).

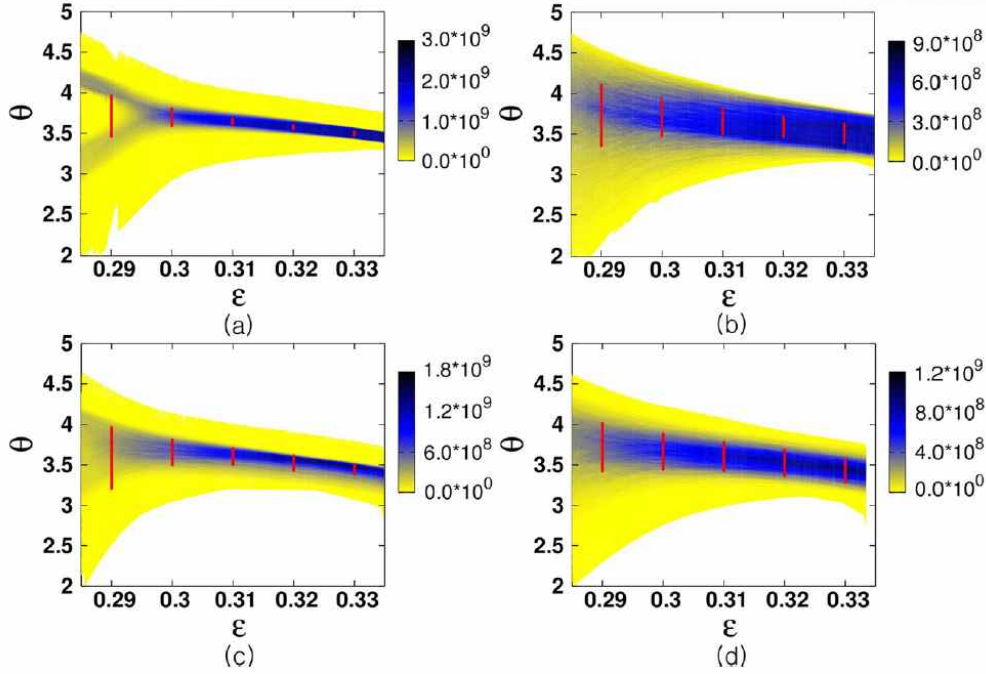


Figure 2.11: The diagram represented energy spread of secondary electron with angular effect, comparing with simulation results and mapping function, where the parameters are (a) $P_n = 64$, $\varepsilon_n = 0.01$ (b) $P_n = 4.2$, $\varepsilon_n = 0.2$ without angular effect and (c) $P_n = 64$, $\varepsilon_n = 0.01$, (d) $P_n = 4.2$, $\varepsilon_n = 0.2$ with effective angular effect.

In Fig. 2.11, the electrons phases mostly reside on the blue region, whose ranges agree well with those measured from the simulations (full width I_{\max}/e). Fig. 2.11 (a), (c) and (b), (d) are comparisons of the phase diagrams when the emission angle is counted [(b), (d)] or not counted [(a), (c)] for parameters corresponding to the cases of Fig. 2.9. In Fig. 2.11 (a) and (c), both measured phases and calculated ones exhibit wider spread when the emission angle is counted, which is a natural result from the broadened effective v_z -spectrum as seen in Fig. 2.9 (a). Note that the bifurcation [two branches of blue region in Fig. 2.11 (a)] is merged out in Fig. 2.11 (c) by the broadened v_z -spectrum by emission angle. In Fig. 2.11 (b) and (d), the phase spread is a little bit wider when the angle effect is counted, which is opposite to the cases (a) and (c). This can be explained by different behavior of effective v_z -spectrum in Fig. 2.9 (a) and (b). In Fig. 2.9 (b), the velocity broadening is not that significant as in Fig. 2.9 (a), but instead, the peak shift to the lower side is severer. We observed from our previous work [4] that when the emission velocity is lower, the phase diagram shifts to the left in $\theta-\varepsilon$ space, which results in narrowing down of phase spread as shown in Fig. 2.11 (d). In other words, depending on peak shift or spectral broadening of v_z -distribution by emission angle, the phase spread (or correspondingly the longitudinal bunch size) can be differently influenced.

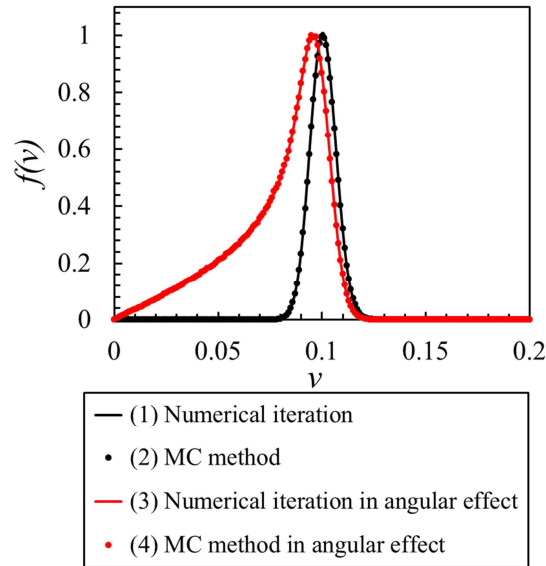


Fig 2.12. Comparison of normalized velocity spectra between MC method and numerical iteration in copper case.

Finally we have considered the case of real parameters of P_n and ε_n for copper, which have much wider secondary energy spectrum as in Fig. 2.12. In this case, when the emission angle is counted, the peak shift appears quite significant ($\Delta v = 0.048$, corresponding to 2.28×10^5 m/s), while the spectral broadening of v_z -distribution is very small. So we can expect, by the same logic discoursed for Fig. 2.11 (b) and (d), the phase spread will be narrowed down. This point could be verified by the measurements from the PIC simulations.

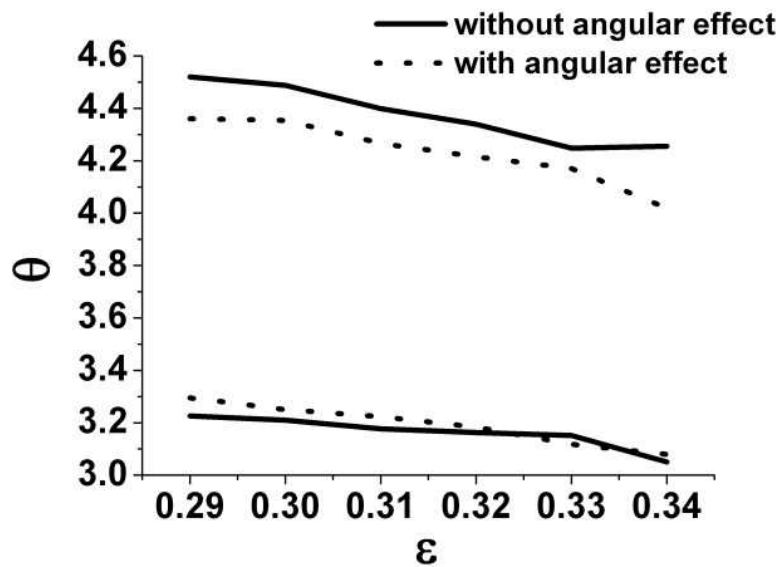


Figure 2.13: PIC simulation of θ area of electron at the copper surface where ε is varied.

In Fig. 2.13, the upper (lower) curves represent the phase maximum (minimum) of electron trajectories as a function of $\varepsilon = E_d / E_a$. As the emission angle is counted (red curves), the phase spread (distance from the lower curve to the upper curve) is narrowed down, which is similar to Fig. 2.11 (b) and (d). The typical value of phase spread for copper is 4.747×10^{-12} sec, corresponding to $80 \mu\text{m}$ in longitudinal bunch size.

2.4 Conclusion

We studied the generation of beam bunching from dc-biased, single-surface multipactor with realistic energy spread and emission angle of secondary electrons. In our previous work, we theoretically studied stability condition of fixed phase and bifurcation, when the energy spectrum of the secondary electrons was quite narrow and the emission angle was neglected. In this paper, we extended our previous work to find the influences of much broader secondary emission spectrum and emission angle, which are always inherent in real materials. What we first considered here was the cases with somewhat artificial material with broad secondary energy spectrum, and emission angle. The novel feature of this work is in employing the effective longitudinal velocity distribution to incorporate the emission angle effect to the one-dimensional quadratic mapping, which we used for theoretical analysis of the electron trajectories. We observed that when the emission angle is counted, the v_z -distribution is effectively widened and simultaneously, there appears peak-shift to the lower side of v_z . These two effects influence the phase spread (or the longitudinal bunch size), sometimes broadening it or sometimes narrowing it down, depending on which of spectral broadening or peak shift is dominant. We also studied the case where the copper, whose secondary spectrum is even wider, was used as an emission plate. In this case also, the bunch size slightly decreased by the emission angle effect: the numerical value of the longitudinal bunch size for copper was $80 \mu\text{m}$, which is suitable for the generation of THz wave generation.

Chapter 3

Design of X-band 6MeV side-coupled linear accelerator

3.1 Introduction

LINAC has been widely applied for medical radiotherapy [16–20], non-destructive imaging [21–23] and various industrial uses [24–26]. In such applications, the electron beam energy at the end of a LINAC waveguide is typically less than 10 MeV and a S-band (~3 GHz) LINAC waveguide is employed in most modern radiotherapy machines. For medical application, majority of radiotherapy machines are composed of several isocentric devices [27–29] including a LINAC waveguide and those are packed in an accurately motion controlled gantry moving around an isocenter on a patient's body. From an engineering point of view to make the gantry system easy to design and manufacture, minimizing the LINAC waveguide is crucial because all of the medical LINACs as well as most of LINACs for industrial applications should be surrounded by a massive radiation shield made of lead. Therefore, an all-in-one LINAC waveguide structure, an assembly of a buncher section and an acceleration section connected with a simple thermionic electron gun, has been adopted. Recently, development of compact LINACs such as C-band (~5.7 GHz) [17,20,28,30–33] and X-band LINACs with a side-coupled cavity waveguide [21] or an axially coupled cavity waveguide [24,34,35] have been the subject of great interest because of their merits as proven by the Cyberknife. In contrast with the machines employing a S-band medical LINAC, the Cyberknife [36] has the most compact medical LINAC, a X-band (9.3 GHz) LINAC, which is connected to a robotic arm. By virtue of its compactness and lightness, the Cyberknife has a high degree of motion freedom owing to such unique configuration employing a robotic arm.

3.1.1 Application of LINAC

A particle accelerator is a device that uses electromagnetic fields to accelerate charged particles to high energy. There are two representative oscillating field accelerators: linear accelerator, circular or cyclic accelerator depending on a direction of particle trajectory. In a linear accelerator (LINAC), particles are accelerated in a straight line with a target of interest at one end. They are often used to provide an initial low-energy kick to particles before they are injected into circular accelerators. The longest LINAC in the world is the Stanford Linear Accelerator (SLAC), which is 3 km long. [63,64]. And the longest LINAC in Korea is Pohang accelerator, which is 170 m long. The above mentioned large accelerators are best known for their use in particle physics as colliders. Other kinds of LINAC are used in a large variety of applications, including particle therapy for oncological purposes and X-

ray imaging, irradiation processing, non-destructive testing. For medical therapy, accelerators require 3~15 MeV pulsed electron beam. And current commercial accelerators are resonated in S-band, C-band and X-band frequency. According to the general feature of LINAC, the volume and length of LINAC is inversely proportional resonant frequency of LINAC.



Figure 3.1: Medical application of LINAC

3.1.2 Property of LINAC

A block diagram shows a LINAC structure with bunching and accelerating cavities, and supplied with electromagnetic energy by an RF power such as klystron, magnetron and so on. Beam is injected from a dc gun. Vacuum system is required for overcoming breakdown and good beam transmission. Electric power supports to DC gun and RF power, vacuum system. A cooling system removes the heat generated by the resistive wall losses of electromagnetic energy and accelerated beam in LINAC structure and it requires for RF power source. To provide efficient acceleration for beam, the beam should be bunched in bunching section.[18]

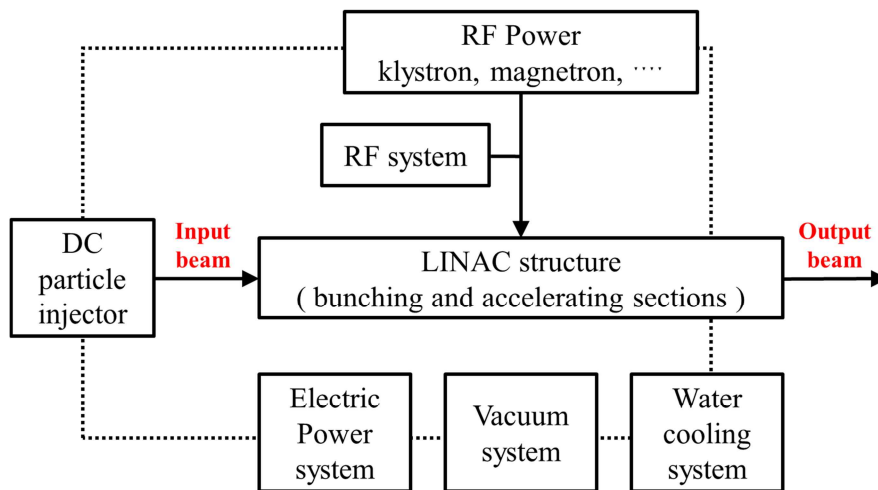


Figure 3.2: A simplified block diagram of LINAC system

$\pi/2$ mode of a chain of coupled oscillators has advantage to devise a suitable geometry satisfying a synchronous condition for particles, and resulting in high shunt impedance. And all of excited cells can contribute acceleration to produce beam energy gain. A better solution for retaining the advantages of the $\pi/2$ mode, while maintain high shunt impedance, is to form a biperiodic chain in which the geometry of the excited accelerating cavities is optimized for best shunt impedance, and the unexcited cavities, also called coupling cavities, are chosen to occupy less axial space and are tuned to the same resonant frequency as the excited cavities. The two most popular geometries that have been invented are the on-axis coupled structure, where the coupling cavities occupy a smaller axial space than the accelerating cavities, and the side-coupled cavity, where the coupling cavities are removed from the beam line, leaving the beam axis completely available to the excited accelerating cavities

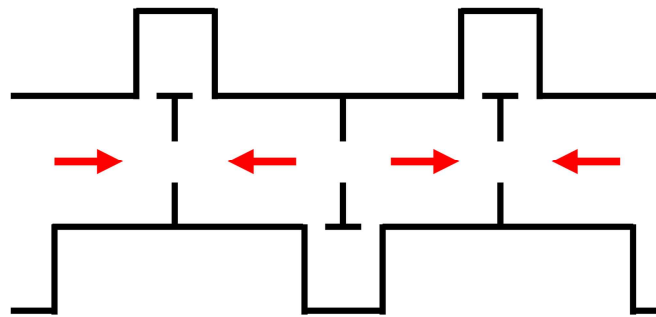


Figure 3.3: Biperiodic standing wave (SW) structures with magnetic side-coupling apertures.

The beam is not simply a medium which absorbs radio frequency (RF) energy and adds an additional resistive load to the cavity, but is really equivalent to a generator, which can either absorb energy from the cavity modes or deliver energy to them. However, in the previous chapters we have assumed that the beam is affected by the cavity, but we have ignored the effects of the beam on the cavity fields. As the beam current increases it becomes important to treat the effects of the interaction between the beam and the cavity more carefully. The effects of the beam on the cavity fields in the accelerating mode are referred to as beam loading. They arise physically as a result of the charges induced in the walls of the cavity as the bunches, together with their commoving electromagnetic fields, pass through the cavity. The induced charges produce fields that act back on the particles in the bunch, and this interaction does work on the particles, which radiate energy to the cavity. In this chapter we introduce these effects through the fundamental theorem of beam loading, which relates the energy delivered to the cavity to the charge q of a single point charge passing through it. The proportionality factor between the energy transferred to the cavity and the squared charge is called the loss factor. The most important effects of beam-induced fields in modes other than the accelerating mode, An external generator is provided to establish the fields needed for acceleration of the beam,

and in which the net field is a superposition of the generator-induced plus the beam-induced fields. When the beam-induced field in the accelerating mode becomes comparable to the field induced by the external generator, the net phase and amplitude will only be satisfactory for beam acceleration, if some means of compensation for the effect of the beam is provided. The conventional analysis of beam loading in a standing-wave cavity, including the conventional method used for compensation, is presented in this chapter 3.2. [18]

3.1.3 Important parameters of LINAC

There are several important parameters of merit which are commonly used to characterize LINAC. Some of parameters depend on the RF power which is dissipated by electrical resistance at the wall of cavities. The quality factor of resonant cavity is defined as

$$Q = \omega U / P \quad (3.1)$$

where P is average power and U is stored energy. And ω is resonant frequency. The shunt impedance is expressed that effectiveness of producing a voltage for deriving Power and defined as

$$r_s = \frac{V_0^2}{P}, r_{s,l} = \frac{V_0^2}{PL} \quad (3.2)$$

$$r'_{s,l} = r_{s,l} T^2 = \frac{(V_0 T)^2}{PL} \quad (3.3)$$

where V_0 is a voltage in beam direction. $r_{s,l}$ is shunt impedance per unit length. $r'_{s,l}$ is effective shunt impedance per unit length (L). T is transit time factor which is defined as

$$T = \frac{\int_0^L E(r, x) \cos(2\pi x / \beta\lambda) dx}{\int_0^L E(r, x) dx} \quad (3.4)$$

where r is radial position. x is beam direction and β is relativistic velocity. In most practical cases the change of particle velocity in the gap is small compared with the initial velocity. If we ignore the velocity change, $\beta\lambda$ is the distance the particle travels in an RF period. The Fig. 3.4 shows axial electric field distributions at unit cell structure of X-band (9.3 GHz) LINAC. Effective electric field is the practical field which affects the traveling electron in an RF period.

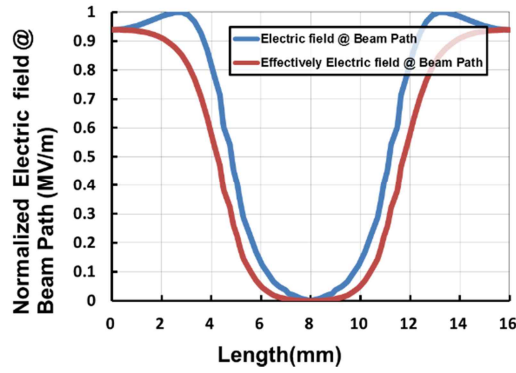


Figure 3.4: Effectively normalized electric field at beam path in unit cell structure

There is two representative coupling of medical LINAC is axial coupling and side coupling type. Figure 3.5 shows the cross section view of side-coupled LINAC to express coupling factor. The relation equation of stored energy between cavities are expressed using equivalent circuit and is defined as

$$\frac{k_i}{2} I_i + I_{i+1} + \frac{k_{i+1}}{2} I_{i+2} = \frac{\omega_{\pi/2}^2}{\omega^2} I_{i+1} \quad (3.5)$$

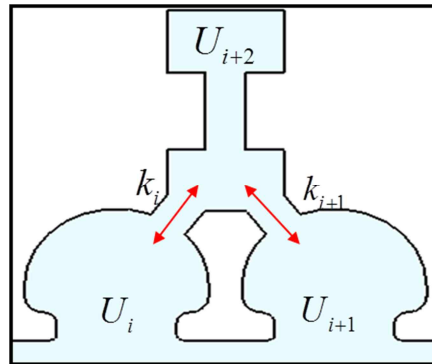


Figure 3.5: Stored energy and coupling coefficient in side-coupled LINAC

When the resonant mode of LINAC is $\pi/2$ mode, the stored energy is defined as $U_{i+1} = 0$, otherwise $I_{i+1} = 0$. Eq. (3.5) is re-expressed as

$$\begin{aligned} \frac{k_i}{2} I_i + \frac{k_{i+1}}{2} I_{i+2} &= 0 \\ k_{i+1} &= k_i \sqrt{\frac{U_i}{U_{i+2}}} \end{aligned} \quad (3.6)$$

3.1.4 Simulation tools

The numerical codes are used in the design of cavities for linear accelerators because the analytical calculations can be used only with simple geometries, as the so called pill-box, which are not useful for real applications. These numerical soft wares are used to optimize the shape of the cavity, given overall dimensions, in order to get the best values for the requested resonant frequency, field pattern and quality factor. Most known and used computer programs for such calculations are:

A Superfish is a frequency domain 2-dimensional simulation which uses a finite elements algorithm. From the practical point of view, after the preparation of a file with the geometry of the structure, one can obtain the resonant frequency for every resonant mode of the cavity, the quality factor and the shunt impedance and other useful parameters. The program has lots of internal macro dedicated to the calculations of parameters useful in the accelerator cavities design as the power dissipated on each wall of the cavity. Other useful results given are the resonant frequency variations for a unit displacement of all the walls of which the cavity is composed.

MAFIA (Maxwell's equation using a Finite Integration Algorithm) is a 3-dimensional code either in the time and the frequency domain. It has a CAD-like interface and it is a powerful general purpose simulation. The later versions have also the relevant possibility of calculation with small losses in the walls.

HFSS (High Frequency Structure Simulator) is a recent product from ANSOFT and is a 3D structure electromagnetic field simulator. It has a CAD-like approach, it offers an intuitive interface to simplify design entry, a field solving engine with accuracy-driven adaptive solutions based on a finite element method (FEM), and a post-processor for pose-elaborations of the calculated fields. The software has also an optimization tool. [65]

CST(Computer Simulation Technology) MWS(MICROWAVE STUDIO) is a specialist tool for the 3D EM simulation of high frequency components. CST MWS included modules based on numerous different methods including finite element method (FEM), method of moments (MoM), multilevel fast multipole method (MLFMM) and shooting boundary ray (SBR), each offering distinct advantages in their own domains. The software has also an optimization tool.

3.2 Fundamental theory and basic study

3.2.1 Design flow

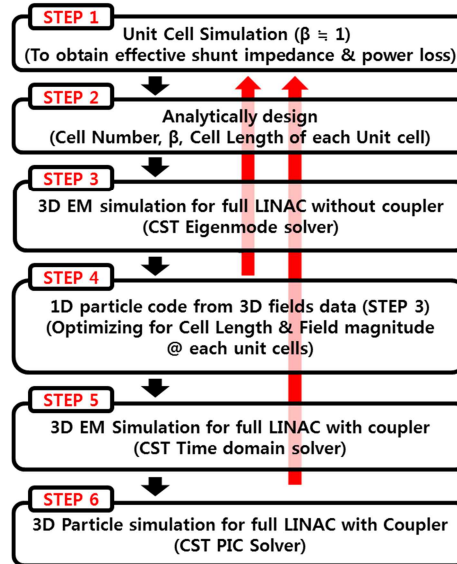


Figure 3.6: Design flow of X-Band LINAC. The red arrows show critical feed-back processes.

The design process of the X-band (9.3 GHz) 6 MeV LINAC waveguide can be divided into 6 steps. In step 1, a unit cell was analyzed by the 3D electromagnetic eigenmode calculation in the CST code. A unit cell is a basic structure which determines physical characteristics of a LINAC waveguide such as shunt impedance, quality factor and coupling factor. In step 2, the analytical calculation follows the equations from Thomas P. Wangler's book [18] and Kamino's paper [28]. The numerically calculated values from step 1 and the assumed values such as RF power are used for the analytical calculations in step 2. The critical values such as the shunt impedance and the number of cells in step 2 comes from step 1 or initial assumption and those are refined several times considering the iterative results in the following steps. In step 3, the eigenmodes in the 3D model of a LINAC waveguide are analyzed. At this step, a simplified model excluding the external RF coupler is used for quick estimation of the physical characteristics of the coupled cavity waveguide. In step 4, a simple 1D particle code developed by us is utilized for quick estimation of electron acceleration. At the first iteration of the steps, the field profiles are given by eigenmode calculations in step 3. And after several iterations, eventually, the field profiles extracted from step 5 are used. The magnitude and the distance (equivalent to the distance between adjacent cavities) of each maximum of electric field are artificially manipulated until an optimized condition for electron beam acceleration are achieved. This step is one of the most important feed-back point because the manipulation of the field profile may demand considerable changes of the design parameters. In step 5, the LINAC waveguide including an external RF coupler is analyzed by 3D time domain calculations. By the calculations, not only the RF coupling level to an external RF power source but also the 3D electric field profiles which is more

realistic than the results from the eigenmode calculations can be obtained. In step 6, PIC simulations of the electron acceleration up to 6 MeV in a 9.3 GHz side-coupled cavity waveguide composed by coupling of 49 cavities are performed. By analyzing the physical properties of the accelerated electrons, validity of the designed values for the cavity waveguide can be verified. The more details of each steps are discussed in the following sections.

3.2.2 Numerical stabilization

A measure of the sharpness of response of the cavity to external excitation is the Q of the cavity which is the time-averaged energy stored in the resonant cavity to the dissipation of power at wall of cavity. And the stored energy decays away exponentially with a decay constant inversely proportional to Q. The time dependence implies that oscillations of the fields in the cavity are damped as follows:

$$E(t) = E_0 e^{-\omega_0 t / 2Q} e^{-i(\omega_0 + \Delta\omega)t} \quad (3.7)$$

where we have allowed for a shift $\Delta\omega$ of the resonant frequency as well as the damping. A damped oscillation such as this has not a pure frequency, but a superposition of frequencies around $\omega = \omega_0 + \Delta\omega$. To express as frequency distribution, the Eq. (3.7) is rewritten as follows:

$$\begin{aligned} |E(\omega)|^2 &\propto \frac{1}{(\omega - \omega_0 - \Delta\omega)^2 + (\omega_0 / 2Q)^2} \\ \text{Re}(E(\omega)^2) &\propto \frac{1}{(\omega - \omega_0)^2 + (\omega_0 / 2Q)^2} \quad (\text{where } \Delta\omega \approx 0) \end{aligned} \quad (3.8)$$

Fig. 3.7 is numerically calculated for the simple pillbox from Eq. (3.8) by CST Time domain solver. The ω_0 of pillbox is 9.3052 GHz.

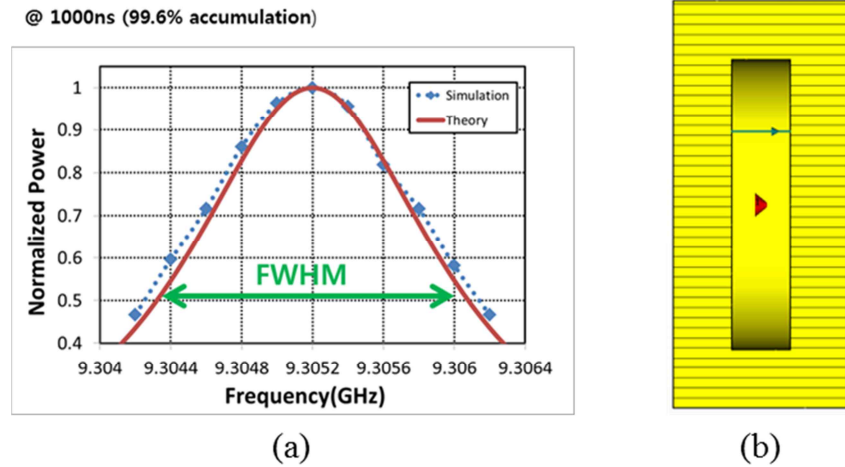


Figure 3.7: (a) Resonance line shape from simulation results of simple cavity and theoretical calculation from Eq. (3.8). The full width at half maximum (FWHM) is equal to the unperturbed frequency ω_0 divided by the Q of the cavity. (b) Cutaway picture of Simple cavity structure. Red arrow is position of RF source in 3D time domain simulation.

If an initial amount of energy is stored in the cavity, it decays away exponentially with a decay constant inversely proportional to Q . The oscillations of the fields in the cavity are damped as follows:

$$\begin{aligned} \text{Re}(E'(t)) &= E_0 (1 - e^{-\omega_0 t / 2Q}) \\ E'(t) &= E_0 (1 - e^{-\omega_0 t / 2Q}) e^{-i(\omega_0 + \Delta\omega)t} \end{aligned} \quad (3.9)$$

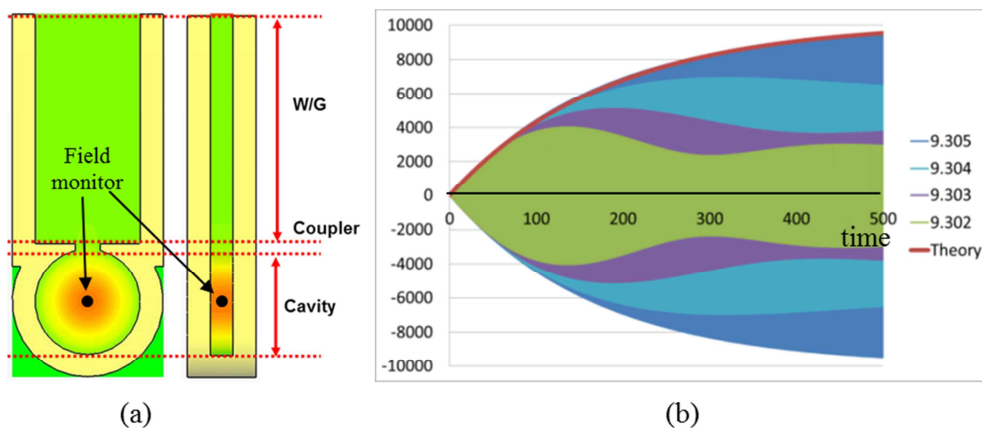


Figure 3.8: (a) Cutaway picture of Simple cavity structure with coupler and (b) Electric field magnitude measured from field monitor in 3D CST MWS time domain simulation and theoretical calculation from Eq. (3.9)

In the numerical analysis, numerical stability is a generally desirable property of numerical algorithms. The CST MWS algorithms are for solving finite differential equations by discrete approximation. Numerical algorithms for differential equations the concern is the growth of round-off errors which might cause a large deviation of final answer from the exact solution. Some numerical algorithms may damp out the small fluctuations (errors) in the input data; others might magnify such errors. Calculations that can be proven not to magnify approximation errors are called numerically stable.

3.2.3 RF breakdown limit for X-band linear accelerator waveguide

Kilpatrick's criterion [66,67] is relevant to the RF breakdown limit, and it is given as follows:

$$f(\text{MHz}) = 1.64E_k^2 e^{-8.5/E_k}, \quad E_b = bE_k, \quad (3.10)$$

where f is the resonant frequency of the LINAC and E_k is the peak electric field at which the RF breakdown can happen. Some research groups had selected E_k of 120 MV/m for C-band (5.712 GHz) [20,28] so that the brave factor (b) of 1.9 can be deduced from Eq. (3.10). For our X-band (9.3 GHz) case, E_k is about 150 MV/m if the same value of b for the C-band LINACs is assumed. In our 3D time domain simulations in step 5, the highest electric field residing around the cavity nose was 107 MV/m when the RF power of 1.6 MW was injected inside of the cavity waveguide.

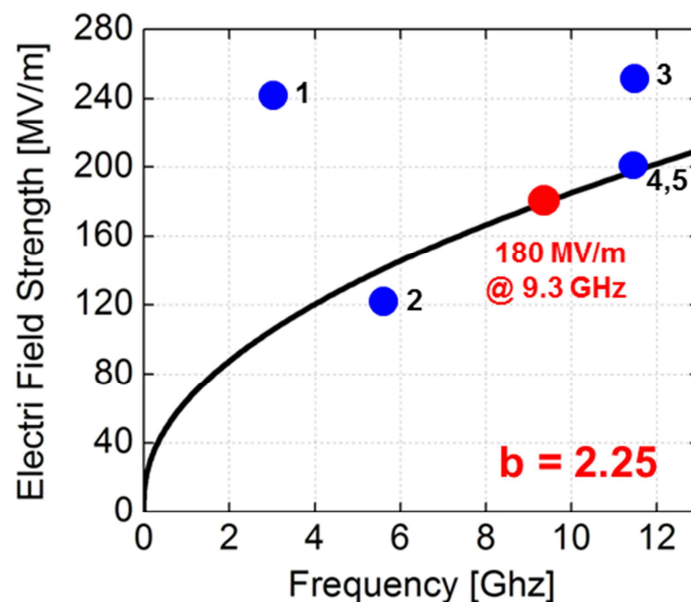


Figure 3.9: Vacuum discharge limit for linear accelerator waveguide

Table 3.1: Vacuum discharge limit of the research group

Resonant frequency	Structure type / Wave type	Vacuum discharge limit	Lab. or Company	Ref.
3GHz (S Band)	LINAC / SW	240MV/m	Varian(1983)	[68]
5.7GHz (C Band)	LINAC / SW	120MV/m (340MV/m)	Mitsubishi(2007)	[69]
11.4GHz (X Band)	Klystron / TW	250MV/m	SLAC	[70]
11.4GHz (X Band)	LINAC / SW,TW	200MV/m	SLAC(2003),	[71]

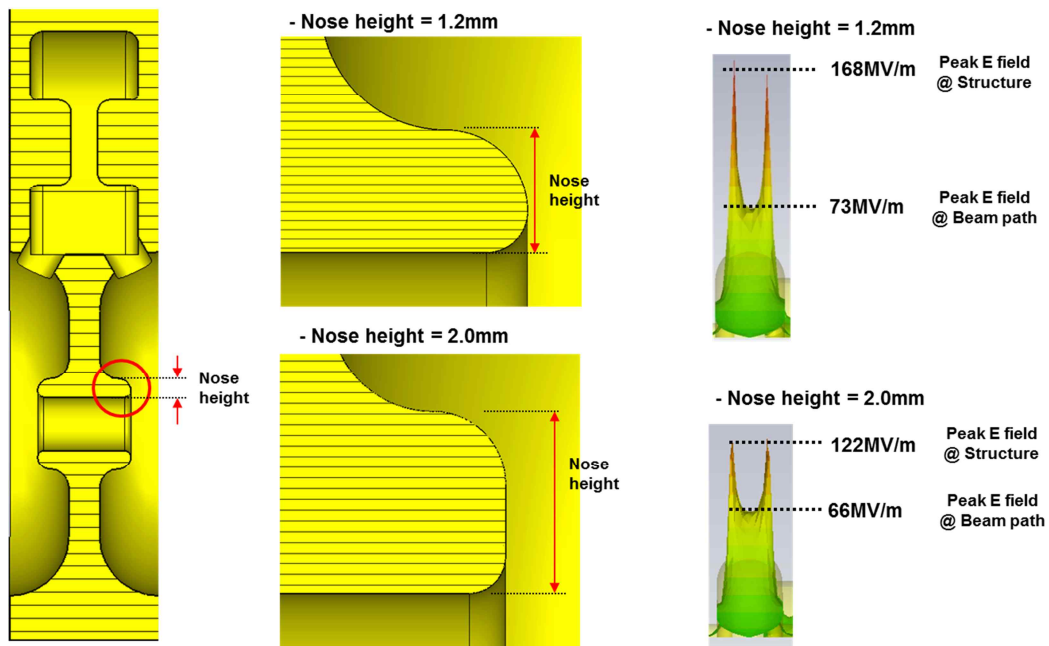


Figure 3.10: Peak electric field decreased by dimensional change of nose part in unit cell structure to avoid vacuum breakdown

3.2.4 Energy gain

To calculate the voltage (energy) gain of an electron beam, the equation referred from Thomas P. Wangler's book [18] given Eq. (2) was used.

$$\begin{aligned} \text{Re}(\tilde{V}_c) &= V_{c,r} = V_g \cos(\phi + \psi) + V_b \cos(\pi + \psi) \\ &= \frac{2\sqrt{\beta}}{1+\beta} \sqrt{P'_g r'_{s,l} LN} \cos \phi \cos(\phi + \psi) - \frac{r'_{s,l} LN}{1+\beta} I_B \cos^2(\psi), \end{aligned} \quad (3.11)$$

where ϕ is the phase ahead angle of the electron bunches from the crest of the accelerating electric field, ψ which was neglected in the Kamino's paper [28] by setting $\psi = 0$ is the detuning angle, P'_g is the RF power, and $r'_{s,l}$ is the effective shunt impedance per length considering the transit time of an electron bunch. The length of a unit cell, the coupling coefficient, and the beam current are denoted as L , β , and I_B , respectively. The second term of Eq. (3.11) comes from the beam loading effect. Because the beam loading effect in the all-in-one LINAC waveguides composed of the buncher section and the acceleration section is hard to predict accurately, neglecting the detuning angle ψ is reasonable. However, in our design process, the 3D PIC simulations were employed mainly in the design step 6 so that the detuning angle was considered for more accuracy. The optimum coupling factor β_o for critical coupling and relevant detuning angle ψ_o were derived by Eq. (3.12),

$$\beta_o = 1 + \frac{r'_{s,l} LN \cos^2 \phi}{V_{c,r}}, \quad \psi_o = \arctan \left(-\frac{\beta_o - 1}{\beta_o - 1} \tan \phi \right). \quad (3.12)$$

Figure 3.11 shows the energy gain of an electron beam corresponding to total number of unit cells, which is calculated by Eq. (2). A generator power of 1.6 MW was assumed because a 9.3 GHz magnetron with 1.7 MW peak power is commercially available. L (d of cell No.5 in Table 3.2) and ϕ were 16 mm and 20° , respectively. Table 3.2 shows the optimized axial lengths of unit cells and 3D eigenmode calculation results for each unit cell. The buncher (low energy) section is composed of the cells numbered from 1 to 4 and the acceleration (high energy) section is composed of 19 cell numbered as 5. The cell numbers were classified by the structural features of each unit cell. And the axial length (d) of unit cells was optimized to match the electron beam velocity (v/c). In addition, the important physical properties, such as the frequency of accelerating cavities (f_a), side coupling cavities (f_{sc}) and the shunt impedance per length (r_s) of each cell are given in Table 3.2. For the cell No. 5 in Table 3.2, the shunt impedance is 200 M Ω /m. The effective shunt impedance per length $r'_{s,l}$ in Eq. (3.11) and (3.12) was 139.4 M Ω /m which was obtained by multiplying the square of transit time factor (0.835). The value of $r'_{s,l}$ needs to be reduced again by considering the reduction factor which was reported as 74 % for the C-band 5.2 MeV hybrid type LINAC [28] and 88 % for the X-band 6

MeV axially coupled LINAC [35]. At the first iteration of our design flow, the reduction factor of 88 % was assumed in step 2. Consequently, after several iterations for optimization and correction, 89.2 M Ω /m of $r'_{s,l}$ was obtained.

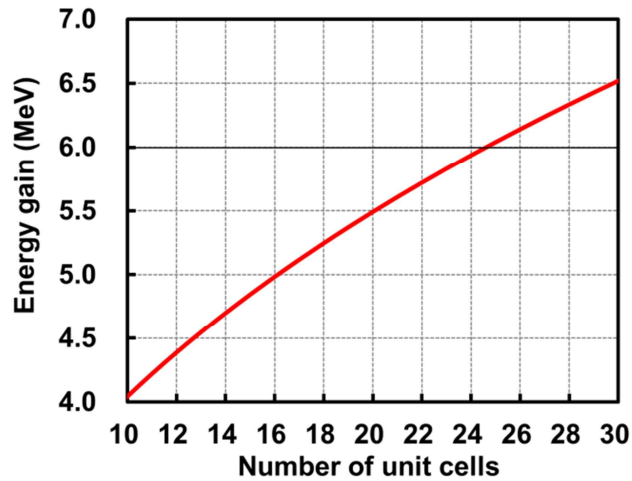


Figure 3. 11: Energy gain of electron beam is calculated by Eq. (3.11), corresponding to total number of unit cells. The required number of cells for 6 MeV acceleration with 70 mA of peak current is 25.

Table 3.2 Given parameters of Eq. (3.11)

	Parameters	value	Unit
f	Resonant frequency	9.3	GHz
P'_g	Generator Power	1.58	MW
ϕ	Phase ahead angle of electron bunches	-20.0	Degree
I_B	Current	70	mA
L	Unit length	16	mm
$r_{s,l}$	Shunt impedance per length	128	M Ω /m
$r'_{s,l}$	Effective shunt impedance per length	89.24	M Ω /m

3.2.5 Unit cell simulation

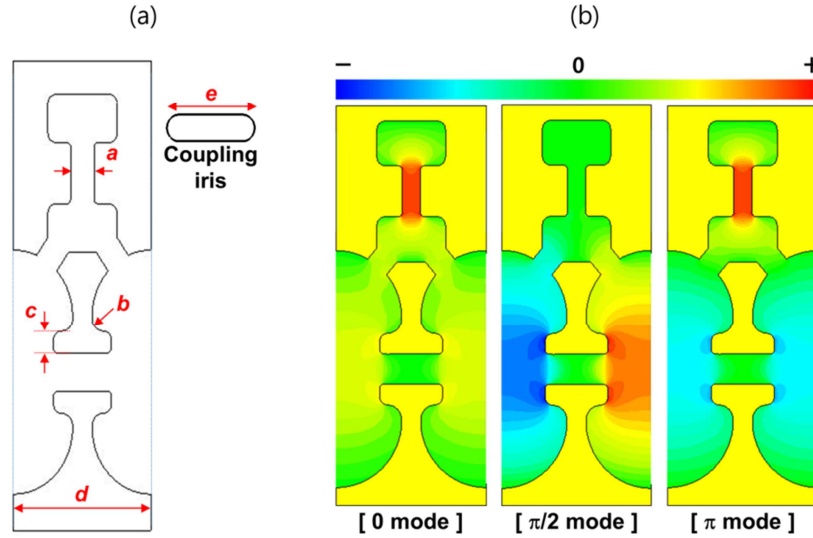


Figure 3.12: (a) Unit cell and full LINAC waveguide with typical values of critical dimension parameters (b) Electric field distributions of 0 mode, $\pi/2$ mode, and π mode in a unit cell extracted from the 3D eigenmode calculations.

Figure 3.12 (a) shows a unit cell structure which is composed of one accelerating cavity (divided into half cavities) and one side coupling cavity. Typical values of the critical dimension parameters and a half cutaway view of the full LINAC waveguide, which is composed of a buncher section (about 6 cells) and an acceleration section (about 19 cells), are also given in Fig.3.12 (a). The eigenmodes in a LINAC unit cell were investigated by using 3D electromagnetic simulations. The basic geometry is similar with those in [21] and [72] which have the side-coupled cavity structure. The eigenmode calculations using the hexahedral spatial mesh were performed by running workstations equipped with 128 Gbytes of RAM working on Intel Xeon E5-2687W Octa-core. By considering the quality factor (Q) of the desired $\pi/2$ mode in the unit cell, we determined the permitted limit for the resonant frequency between each cavities. When RF power is applied into a resonant cavity, the stored energy (W) in the cavity depends on the frequency and the quality factor, as $W \propto 1 / \{(\omega - \omega_0)^2 + (\omega_0 / 2Q)^2\}$, where ω_0 is the resonant frequency of the cavity, and ω is the RF frequency derived from a generator. In the case of cell No. 5 in Table 1, with a Q value of 8398 and resonant frequency of 9.3 GHz for $\pi/2$ mode, the full width at half maximum (FWHM) of W was calculated as 1.78 MHz. Therefore, the frequency differences between each neighboring cavity were set to be smaller than a half of 1.78 MHz. Additionally, the calculation error for resonant frequency was also set to be smaller than a half of 1.78 MHz by adjusting the mesh or the iteration numbers of

the computer calculations. Adjusting parameters b and c defined in Fig. 3.12 (a) dominantly affects the resonant frequency of the acceleration cavities f_a . And the resonant frequency of the side-coupling cavities f_{sc} can be dominantly manipulated by the parameter defined as a . The nominal frequency difference between neighboring unit cells is about 0.4 MHz, which is smaller than our permitted limit, a half of 1.78 MHz. The electric field distributions of three different eigenmodes, 0 mode, $\pi/2$ mode, and π mode, extracted from the 3D eigenmode calculations are given in Fig. 3.12 (b), where the electric fields are described on the half cross section of the unit cell labelled as cell No. 5 in Table 1. The number of mesh elements was 1,529,280, and the calculation time was about two and a half hours.

In numerical calculation, frequency error has to be under permitted limit while the mesh cell number is increased. The Fig. 3.13 and 3.14 show numerical stable when number of mesh is above 8×10^6 and 1×10^4 using hexahedral spatial mesh and tetrahedral spatial mesh, respectively.

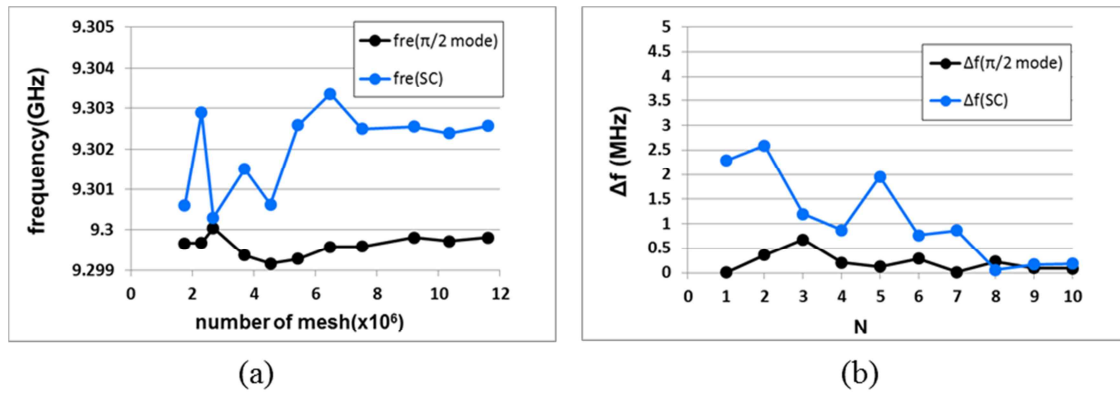


Figure 3.13: (a) Resonant frequencies and (b) frequency deviation, $|f_{N-1} - f_N|$, at $\pi/2$ mode in 3D eigenmode solver while mesh number is swept. The simulation is solved using hexahedral mesh for unit cell structure of X-band LINAC waveguide.

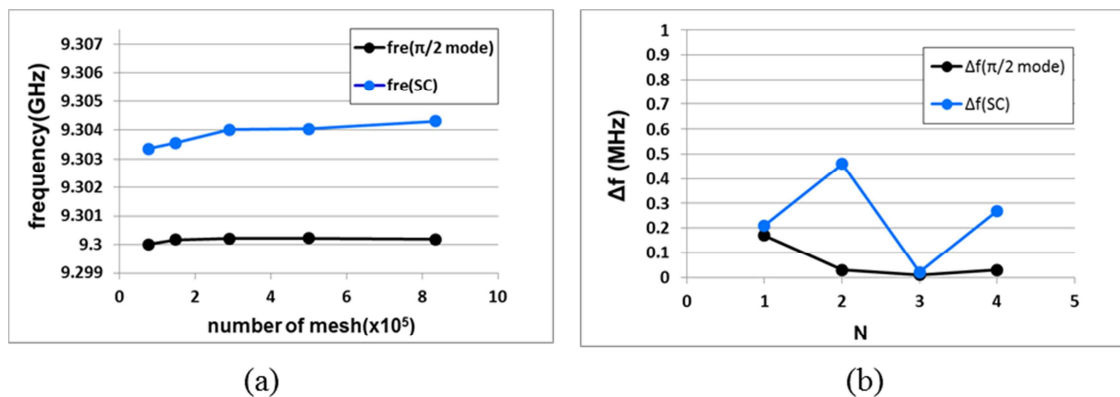


Figure 3.14: (a) Resonant frequencies and (b) frequency deviation, $|f_{N-1} - f_N|$, at $\pi/2$ mode in 3D eigenmode solver while mesh number is swept. The simulation is solved using tetrahedral spatial mesh for unit cell structure of X-band LINAC waveguide.

eigenmode solver while mesh number is swept. The simulation is solved using tetrahedral mesh for unit cell structure of X-band LINAC waveguide.

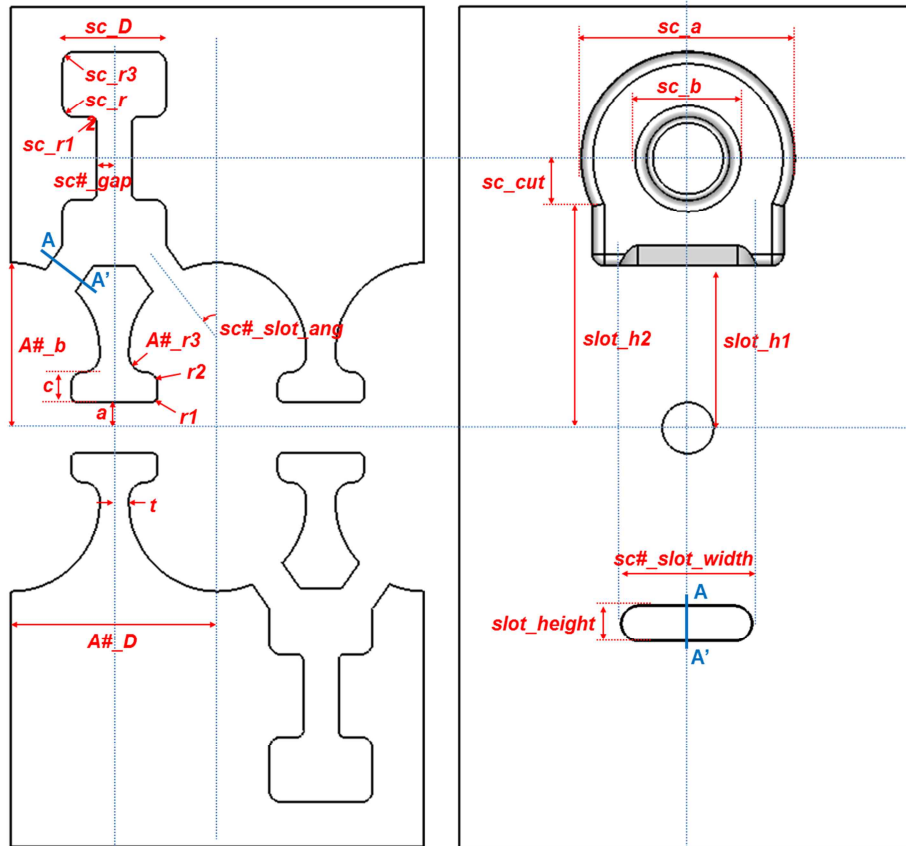


Figure 3.15: Design parameters of X-band 6 MeV LINAC waveguide where # is cell number.

Table 3.3 Important parameters of 3D eigenmode calculation results for unit cells

Cell No. (quantity)	v/c	d (mm)	b	$r3$	$slot_ang$	sc_gap	$slot_width$
1 (1 piece)	0.65	10.477	11.17	1.1273	30	0.9291	9.3
2 (2 pieces)	0.784	12.640	12.180	0.8818	40	0.9314	9.000
3 (2 pieces)	0.888	14.313	12.180	1.2110	40	0.9378	9.510
4 (1 pieces)	0.931	15.004	12.180	1.3430	40	0.9423	9.872
5 (19 pieces)	0.993	16.000	12.180	1.5682	40	0.9410	9.800

Table 3.4 3D eigenmode calculation results for unit cells

Cell No. (quantity)	f_a (GHz)	f_{sc} (GHz)	k	Q	r_s (M Ω /m)	P_{loss} (MW)
1 (1 piece)	9.30001	9.30015	3.047%	6448	140.0	9.062
2 (2 pieces)	9.29999	9.30023	3.086%	7730	182.3	7.559
3 (2 pieces)	9.29983	9.30004	2.988%	8113	193.6	7.202
4 (1 pieces)	9.29997	9.29979	3.076%	8237	196.7	7.090
5 (19 pieces)	9.30037	9.29969	2.782%	8398	200.4	6.950

3.2.6 Optimization of linear accelerator

Shunt impedance (r_s) and quality factor (Q) are important values to represent a performance of a LINAC cavity waveguide. Generally a performance of the cavity waveguide is improved when r_s and Q is higher. Table 3.5 represents sensitivity of important characteristic values by changed dimensional parameters in unit cell cavity (cell No.5) in Table 3.3. Adjusting parameters $r3$ and b defined dominantly affects the resonant frequency of the acceleration cavities f_a . And the resonant frequency of the side-coupling cavities f_{sc} can be dominantly manipulated by the parameter defined as sc_gap . Adjusting parameters c and $r3$ dominantly affects Q and r_s . And slot_width is dominantly affect coupling coefficient. (see Fig. 3.15 and Table 3.5-6)

Table 3.5 Variation of important characteristic values by changed dimensional parameters in unit cell cavity (cell No. 5) in Table 3.3.

Parameter	Variation of characteristic values				
	Δf_a [MHz/ μ m]	Δf_c [MHz/ μ m]	ΔQ [μ m]	Δr_s [M Ω /m $\cdot\mu$ m]	k [%/ μ m]
r3	-0.7016455	0.0020987	1.7409550	0.0222399	-0.0000026
b	-0.7546129	-0.0287247	0.1474368	-0.0040755	0.0000040
c	-0.2031633	-0.0046841	-0.0385605	-0.0219342	0.0000009

sc_gap	0.0003361	3.5449880	-0.1042993	-0.0023733	0.0000094
--------	-----------	-----------	------------	------------	-----------

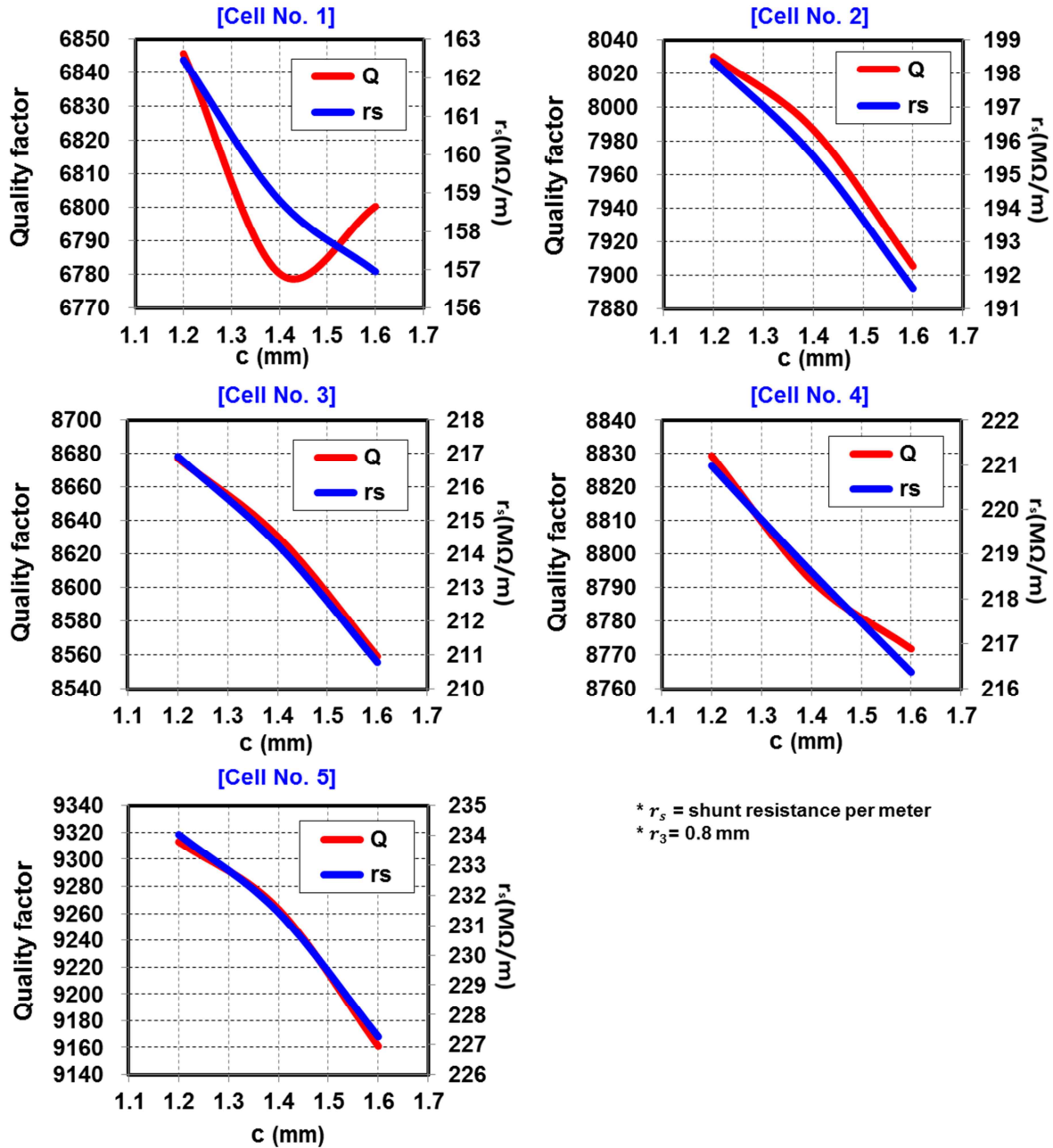


Figure 3.16: Quality factor and shunt impedance by adjusting nose height (c) with $r_3 = 0.8$ mm (see Fig. 3.15) of each unit cells in Table 3.3

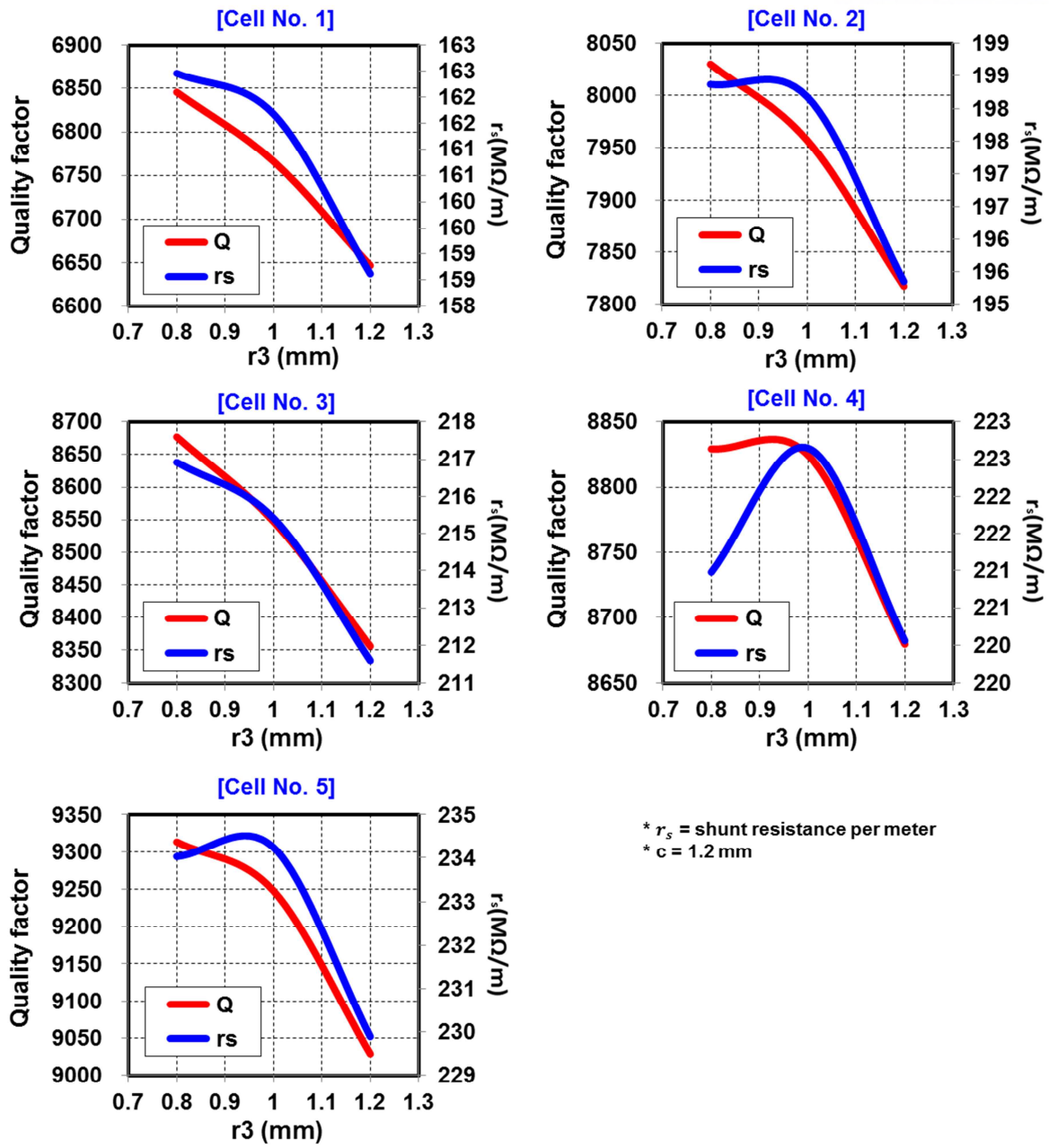


Figure 3.17: Quality factor and shunt impedance by adjusting c with r_3 with $c = 1.2$ mm (see Fig. 3.15) (see Fig. 3.15) of each unit cells in Table 3.3

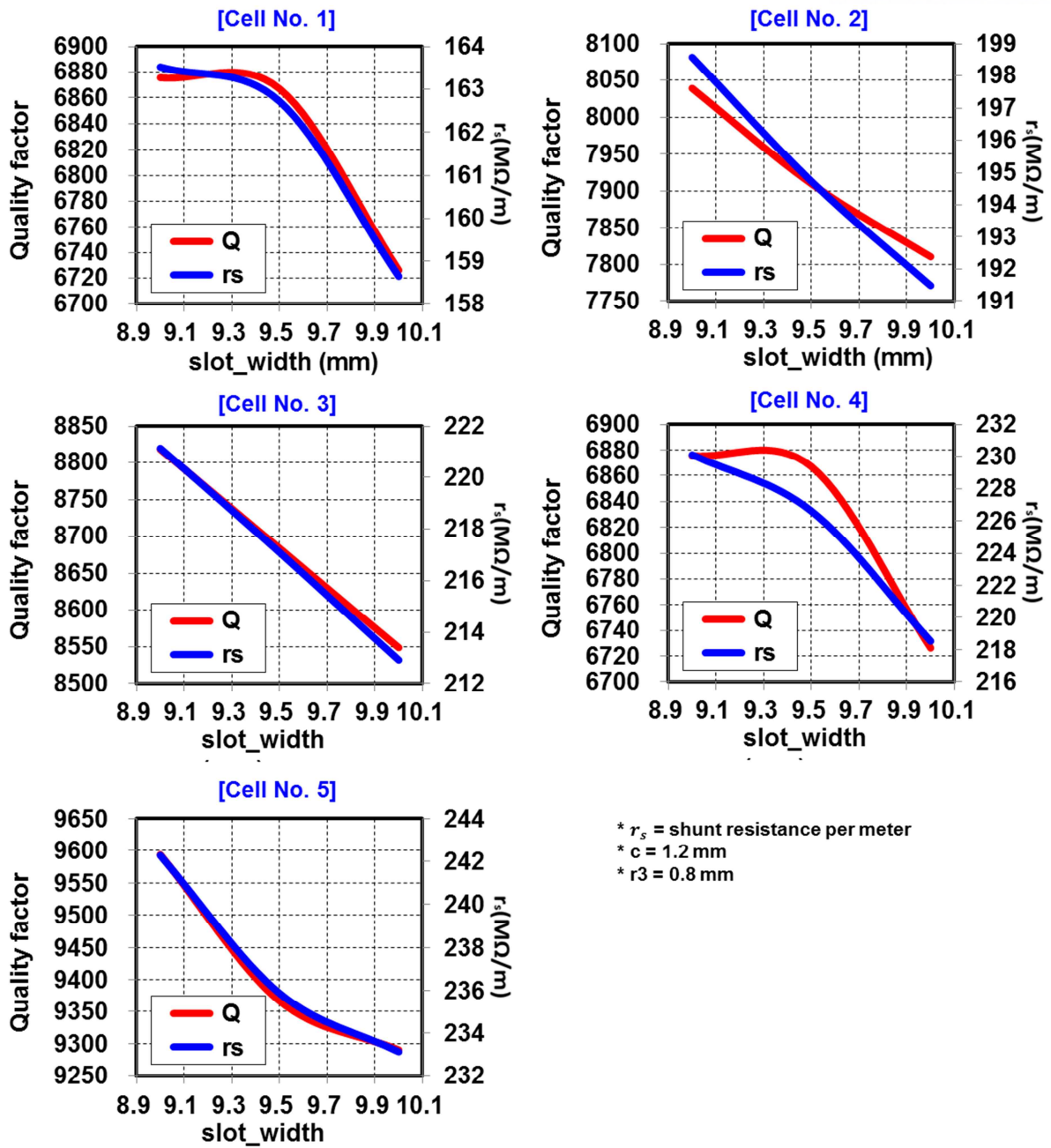


Figure 3.18: Quality factor and shunt impedance by adjusting *slot_width* with $c = 1.2$ mm and $r_3 = 0.8$ mm (see Fig. 3.15) of each unit cells in Table 3.3

3.2.7 Electromagnetic simulation for X-band full LINAC cavity waveguide

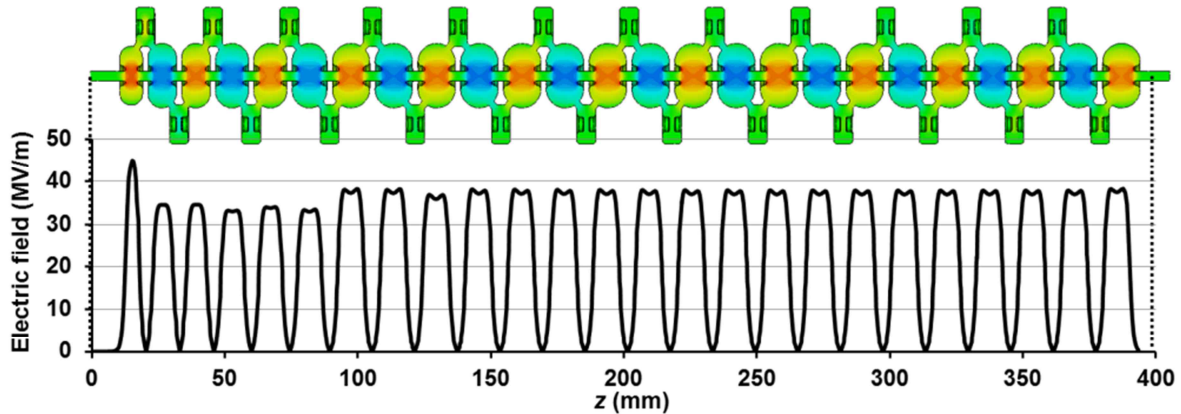


Figure 3.19: The electric field distribution obtained by 3D time domain calculations for a LINAC waveguide comprising 25 accelerating and 24 side-coupling cavities is presented.

The upper figure in Fig. 3.19 shows the electric field configuration on the half cross section of a 9.3 GHz side-coupled LINAC waveguide. Coinciding with the phase variation in the $\pi/2$ standing wave mode, the phase of the electric field is periodically alternating. The curve in the lower figure obtained by the time domain calculations using the hexahedral spatial mesh for a LINAC waveguide including an external RF coupler describes the absolute value of axial electric field at the central line of the beam tunnel. As mentioned in the previous section, the RF power of 1.6 MW was applied for each calculation. When the number of mesh elements was 97,365,120, the calculation time was about 4 days with supplement of a Tesla K40c graphic processing unit (GPU) to the workstations. The resonant frequency of 9.2976 GHz for the $\pi/2$ standing wave mode, about 2 MHz of frequency shift from the unit cell frequencies given in Table 1, was found. In the time domain simulations, the RF power was coupled through an external coupler with -13.74 dB coupling level.

The electric field profiles extracted from the 3D field simulations were employed in the 1D particle code simulations. The code is based on single particle analysis that quickly estimates the axial position and energy gain of each electron. Each electron starts at different RF phases. The phase interval was uniformly set as 0.05° and the initial energy of electrons was 20 keV. By rigorously adjusting the field crests, an optimized electric field distribution for electron beam acceleration up to 6 MeV could be found. The optimized electric field distribution was rebuilt in the 3D field simulations and finally its validity was confirmed by the 3D PIC simulations.

3.2.8 3D PIC simulation for X-band full LINAC cavity waveguide

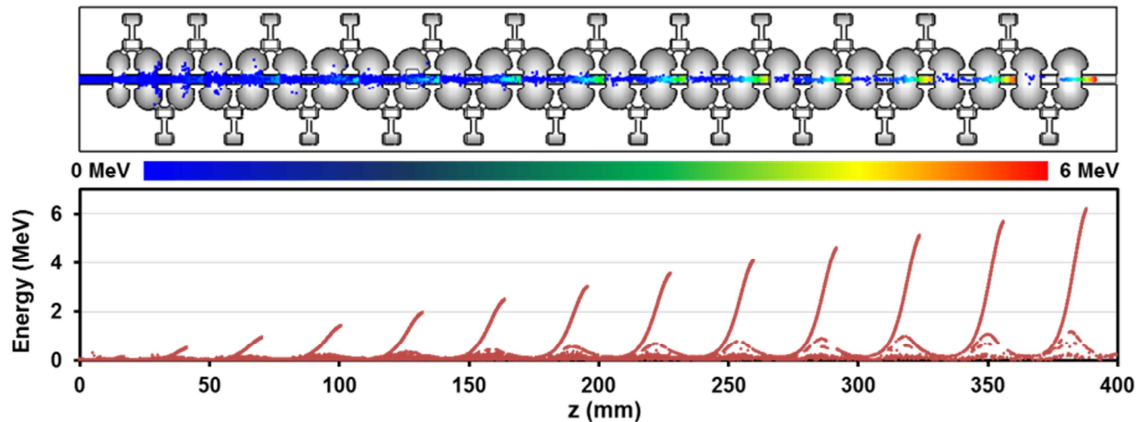


Figure 3.20: In the upper figure, a stream of electrons is shown on the half cross section of a 9.3 GHz side-coupled LINAC. At the right end of the LINAC, an electron bunch with average energy of 6 MeV is escaping the beam tunnel. The lower figure shows the phase space diagram of electrons.

The electron beam dynamic in a side-coupled LINAC waveguide was analyzed by using a 3D PIC code in CST PS. The RF field profiles which were extracted from 3D time domain calculations were downscaled by considering the RF power reduction caused by the energy transfer from RF to electrons. After several iterations of the calculations, we found that about 0.36 MW of RF power was transferred to the electrons for increasing kinetic energy of electrons. Both the electrons escaping through the beam tunnel with relatively high kinetic energy and the electrons colliding on the beam tunnel or the cavity wall were included in the estimation of the energy transfer. Consequently, the electric field profile corresponding to 1.6 MW was downscaled and it was embedded in the LINAC waveguide for the PIC simulations. By virtue of the pre-downscaling of RF power, the transient process of energy transfer from RF to electrons could be quickly skipped. Without the downscaling of RF power, the PIC simulations would be quite time-consuming because the required time to reach steady state is considerably long compared with the computational time step. As for the electron beam, 0.12 million macro particles with 20 kV and 300 mA were injected into the beam tunnel at the front end of the buncher section with the beam filling factor of 37%. The upper figure in Fig. 3.20 shows a typical snapshot obtained from the PIC simulations. The lower figure shows the phase space diagram of electrons describing energy distribution of macro particles along with the direction of the beam tunnel.

Figure 3.21 shows the number of electrons corresponding to their energy. The 3D PIC simulation result shows a peak with the FWHM of 0.35 MeV. The total escaped beam current is 68.5 mA, and electrons relevant to 42.5 mA have the kinetic energy ranging from 5.7 to 6.3 MeV while, initially, the beam current of 300 mA is injected. Transverse emittance at the exit of the LINAC waveguide was

1.51 mm mrad. It was defined as $\varepsilon_r = \sqrt{\varepsilon_x^2 + \varepsilon_y^2}$, $\varepsilon_x = \sqrt{\langle x^2 \rangle \langle x'^2 \rangle - \langle xx' \rangle^2}$, $\varepsilon_y = \sqrt{\langle y^2 \rangle \langle y'^2 \rangle - \langle yy' \rangle^2}$, where x and y are the transverse distance from the beam center in each orthogonal direction, and $x' = dx/dz$, $y' = dy/dz$, $dz \approx \sqrt{dx^2 + dy^2 + dz^2}$. The beam radius is 0.18 mm. It was defined as

$\sigma_r = \sqrt{\sum_{i=1}^N (\langle r \rangle - r_i)^2 / N}$ where r is the transverse particle distance from the beam center and N is the number of macro particles.

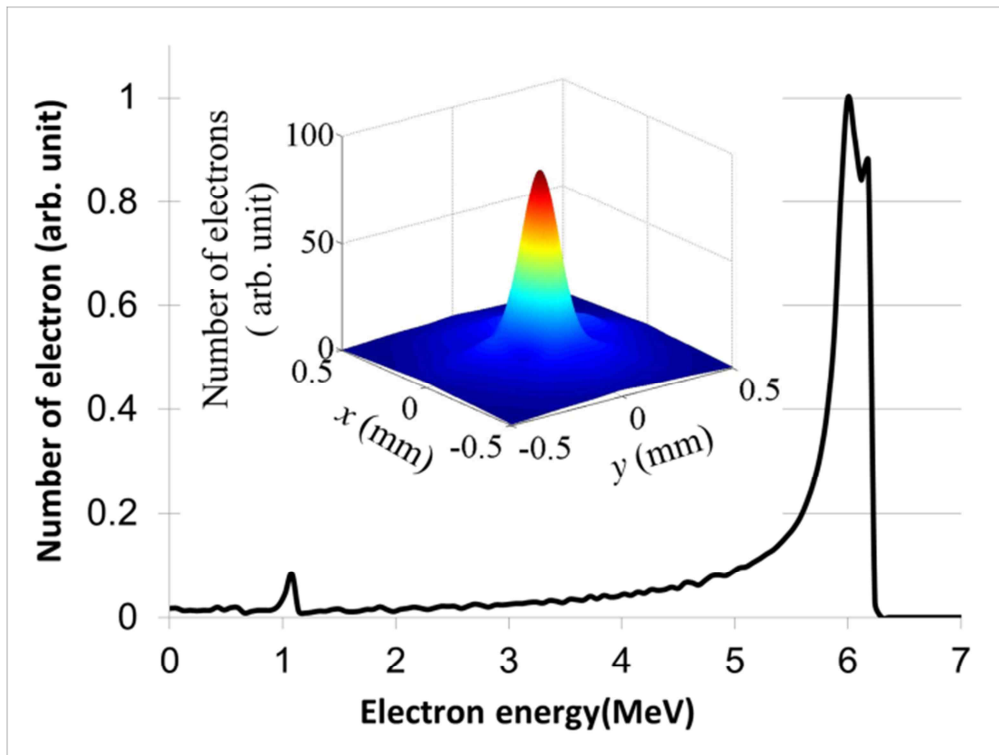


Figure 3.21: Energy spectrum of electrons calculated by 3D codes and emitted electron density at the end of the LINAC waveguide.

3.3 Fabrication

The fully coupled LINAC waveguide consists of an RF port, vacuum port, and 49 coupling and accelerating cavities, as shown in Fig. 3.22. The 49 cavity pieces and the 2 ports in Fig. 3.22 (a) are made of oxygen-free high conductivity copper (C1011 Class F). All of the components in Fig. 3.22 (a) are brazed and the brazed full LINAC waveguide is shown in Fig. 3.22 (b). The inner surfaces of the accelerating and coupling cavities are mechanically processed to reduce the discharge risk by fabricating below $\pm 10\mu\text{m}$ of precision and $0.05\ \mu\text{Ra}$ and $0.025\ \mu\text{Ra}$ of surface roughness for the milling and turning machining, respectively. Insides of the coupling and accelerating cavities were fabricated by a milling machine and a turning machine, respectively, at a constant room temperature of $22\ ^\circ\text{C} \pm 0.1\ ^\circ\text{C}$ in a class 10,000 clean room.

The brazing process can be divided into 4 steps. The filler materials, which have lower melting points, are used in later steps. In step 1, the cavity blocks for bunching and acceleration are combined, and in step 2 the brazed cavity waveguide, vacuum port, and RF port are combined. In step 3, the flanges made of stainless steel are brazed, and in the last step the cooling pipes are added.

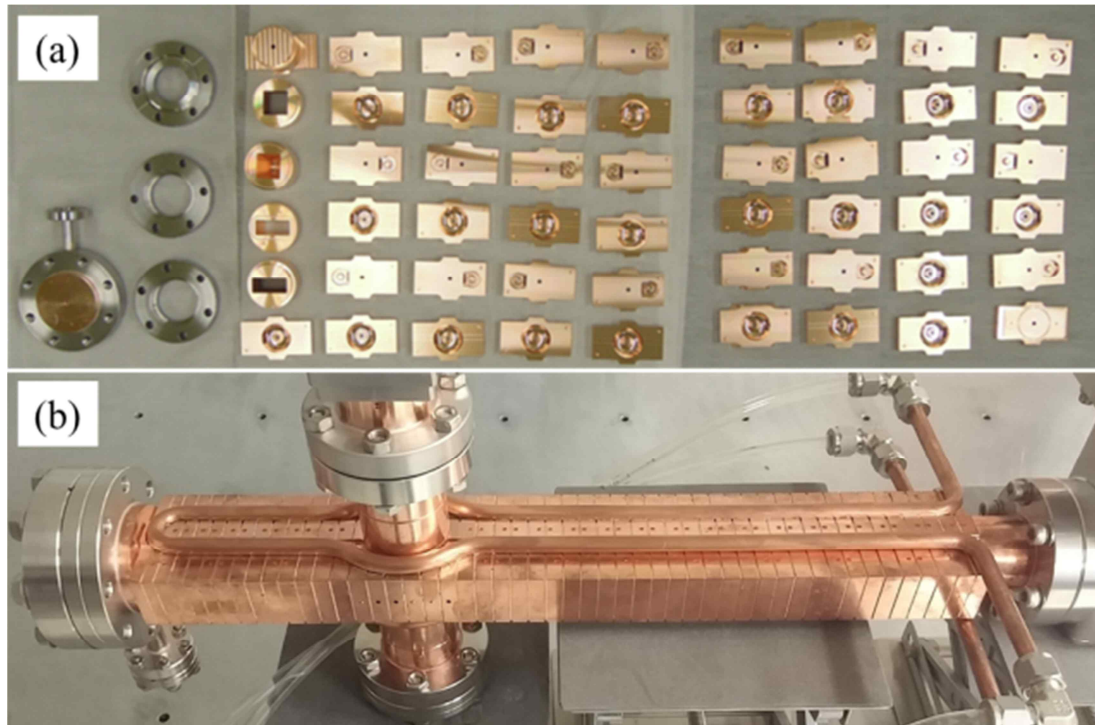


Figure 3.22: Prototype of the X-band 6 MeV side-coupled LINAC waveguide

As possible as higher machining accuracy is more advantage to design any LINAC. However, there is limitation of machining accuracy. And higher accuracy causes higher cost of fabrication. To find proper machining accuracy, we defined the equation as followed:

$$\Delta l \approx \lambda \frac{\Delta f}{f} = c \frac{\Delta f}{f^2} = c \frac{\Gamma}{f^2} \quad (3.13)$$

where Γ is full width half maximum which is measured in response of the cavity to external excitation, c is speed of light, λ is wavelength of resonant frequency. Δl is machining error for fabrication of LINAC. In our case, the resonant frequency is 9.3 GHz, when Γ is about 0.5 ~ 1 MHz, Δl is 1.7 ~ 3.4 μm .

Table 3.6 Deviation (D) and error ($\langle \varepsilon \rangle$) in Eq. (3.15) of designed value in draw for fabrication and measured value of cell No.5 in Table 3.3. Number of products (N) is 15.

Parameter (cell No.5 in Table 3.3)	Drawing value		Measurement value	
	value (mm)	Tolerance (μm)	$\langle \varepsilon \rangle$ (μm)	D (μm)
$D / 2$	8.00	± 10	6.7	7.1
$2(a + c)$	7.50	± 10	1.3	1.9
$2b$	24.36	± 10	4.5	4.9
$(D - t) / 2$	7.00	± 10	1.0	1.0
$sc_D / 2$	3.50	± 10	1.3	1.5
sc_gap	0.949	± 3	2.3	2.8
$sc_a/2 + sc_cut + slot_h2 - slot_h1$	14.485	± 10	6.2	6.8
sc_b	5.57	± 10	6.8	7.2
$sc_cut + slot_h2$	18.25	± 10	1.4	2.1
$2\sqrt{(sc_a/2)^2 - (sc_cut)^2}$	12.978	± 10	7.0	9.2
$r2$	0.80	± 10	1.0	1.0
Y	59.0	± 20	3.0	3.4

Deviation (D) and Error (ε) are defined as

$$D = \sqrt{\frac{\sum_i^N (x_o - x_i)^2}{N}} \quad (3.14)$$

$$\langle \varepsilon \rangle = \frac{\sum_i^N |x_o - x_i|}{N} \quad (3.15)$$

where x_o, x_i are designed and measured values, respectively. And N is number of products.

3.4 Cold test

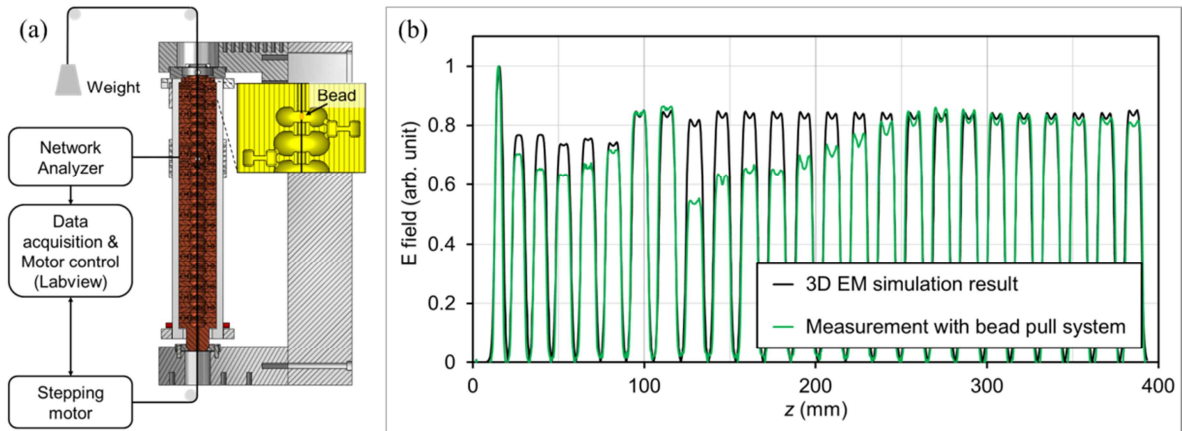


Figure 3.23: (a) Bead pull system diagram, (b) Electric field distribution of 3D EM simulation results and measurements with bead pull system.

The experimental measurement setup for electric field analysis is shown in Fig. 3.23. The LabView controls a stepper motor and obtains S-parameter data through the RF coupler by communicating the network analyzer, Agilent Technologies E5071C. The simulated and measured coupling levels were -13 dB and -11dB respectively. Polypropylene and nylon strings have dielectric constants of 2.2 and 3~3.5, respectively. Several diameters of the strings were tried in the range of 100 ~ 260 μm . A lower dielectric constant and smaller string diameter are better for accurate measurement to minimize the string filling effect [73]. Therefore, polypropylene with a diameter of 100 μm and dielectric constant of 2.2 was chosen for the string. The bead was made of copper, and it was 1.0 mm long with a diameter of 1.0 mm. When the electric field was measured by the bead pull test, the temperature of the

LINAC was kept at $22^{\circ}\text{C} \pm 0.1^{\circ}\text{C}$ by a water cooling system. Even if the optimized bead and string were selected and the temperature of the LINAC waveguide was kept constant, there is still a small fluctuation of data caused by the stepper motor and cooling system. The S-parameter data was collected 100 times at the same position and the mean value of the data was chosen, while the bead was moved each 0.5 mm deviation by the stepper motor.

For the bead pull test, Slater's theorem with perturbation technique [18,74] was used. This measurement is based on the fact that a small perturbing object such as a bead changes the stored energy in the cavity. When the bead is located between the noses of accelerating cavities, the bead changes the capacitance of the cavity. The capacitance is inversely proportional to the square of the resonant frequency, $f \propto \sqrt{1/LC}$. The change of stored energy is proportional to the change of frequency, $\Delta f \propto \Delta U$. Therefore, the frequency shift is proportional to square of the electric field, $E \propto \sqrt{\Delta f}$. The measurement with the bead pull system is shown in Fig. 3.28 (b) with 3D time domain simulation results by CST MWS. To directly compare the computational results and the experimental results, the electric field distribution was measured without any mechanical tuning. The difference between the simulation and measurement results can be noticeable at some positions. However, we believe that the discrepancy is quite small because any cavity in the waveguide was not mechanically tuned during fabrication, brazing, and bead-pull test. As far as we know, without the mechanical tuning, it is hard to build up clear $\pi/2$ standing wave mode in an X-band 6 MeV side-coupled LINAC waveguide.

Table 3.7 RF characteristics of X-band full LINAC cavity waveguide reflected by (a) designed value, (b) drawing value, (c) the value measured by 3D coordinate-measuring machine from 3D time domain simulation in CST MWS and (d) VNA measurement value

Parameters	Initial design value	Drawing value	3D structure measurement value	VNA measurement value
$S_{11,min}$	0.3217	0.2744	0.2966	0.2516
β	0.5132	0.5694	0.5426	0.5979
$f_{\pi/2}$	9.29481	9.29621	9.29340	9.28434
Q_L	4307	4042	4224	4464
Q_o	6517	6343	6516	7133
$r_s (M\Omega/m)$	128.7	115.9	121.2	

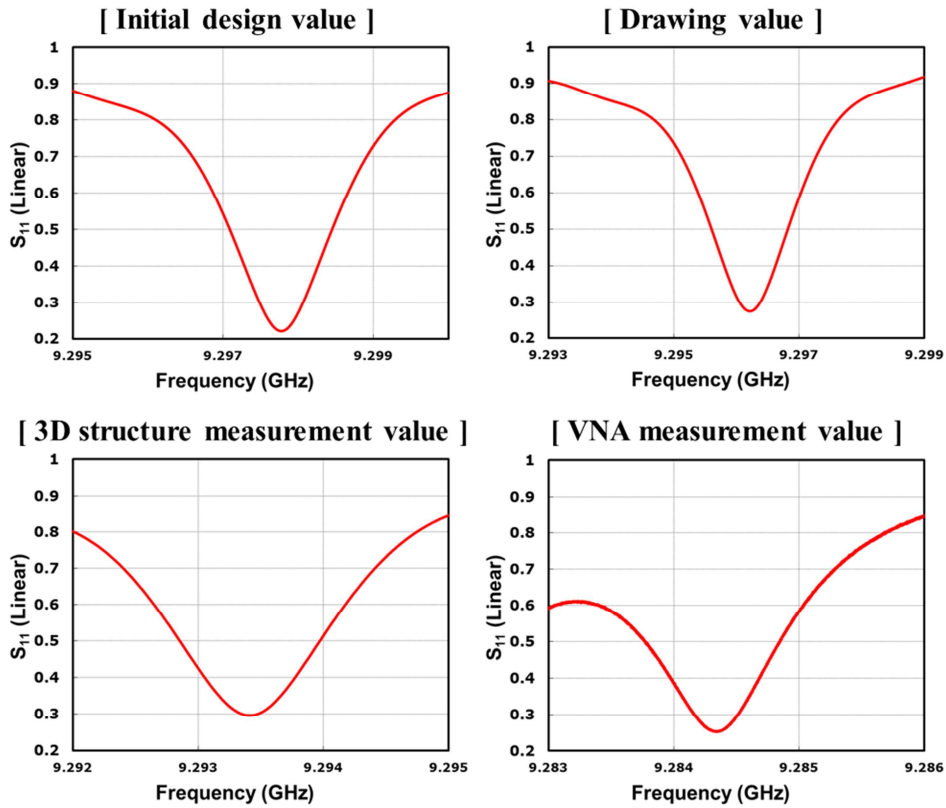


Figure 3.24: S-parameters of X-band full LINAC cavity waveguide reflected by (a) designed value, (b) drawing value, (c) the value measured by 3D coordinate-measuring machine from 3D time domain simulation in CST MWS and (d) VNA measurement value.

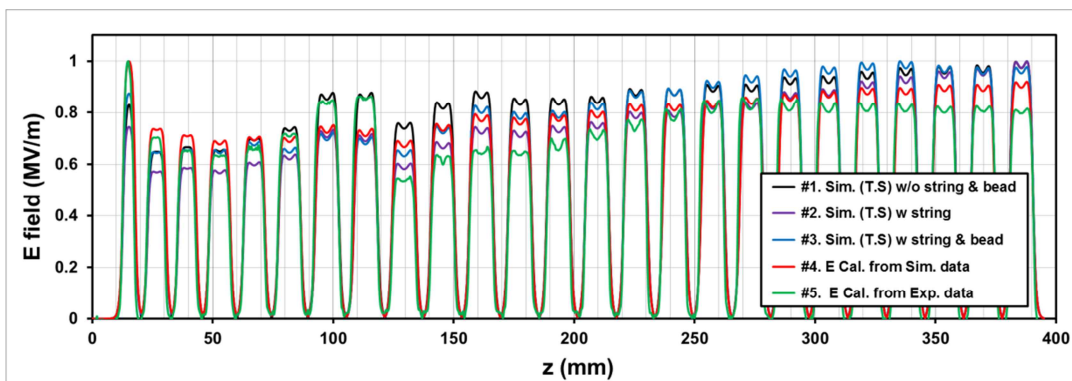


Figure 3.25: Comparison of normalized electric distributions between 3D simulation results and experiment by bead pull of X-band 6 MeV full LINAC cavity waveguide

In Fig. 3.25, “#1. Sim. (T.S) w/o string & bead” is 3D Simulation results without a string and a bead by Time domain solver (CST MWS). “#2. Sim. (T.S) w string” is 3D Simulation results with only string by Time domain solver (CST MWS), “#3. Sim. (T.S) w string & bead” is 3D Simulation results with string and bead by Time domain solver (CST MWS). The data is obtained by locating the

bead at each center position of cavities. “#4. E Cal. from Sim. Data” is electric field calculation ($\sqrt{|f_{b,n} - f_s|}$) from simulation data where $f_{b,n}$ is the frequency from Sim. (T.S) w string & bead (data from #3) obtained by moving the bead through each cells ($n = 1, 2, 3 \dots 25$), f_s is the frequency from Sim. (T.S) w string (data from #2), “#5. E Cal. from Exp. Data” is electric field calculation $\sqrt{|f'_{b,n} - f'_s|}$ from experiment data where $f'_{b,n}$ is measured frequency of LINAC with string and bead through moving the bead at each cells, f'_s is measured frequency of LINAC with only string. For the measurements, a network analyzer, Agilent technologies E5071C, was used. The maximum values of each field patterns are normalized to be one.



Figure 3.26: Experiment setting for measuring S-parameter and electric field distribution by bead pull of X-band 6 MeV LINAC waveguide

3.5 Conclusion

A computational design process for a 9.3 GHz (X-band) 6 MeV side-coupled LINAC waveguide has been developed. The design process contains 3D calculations of an entire structure of the LINAC waveguide. After refining the design process several times, the computational process could predict an optimized configuration for the cavity waveguide within reasonable time and accuracy. A train of electron bunches accelerated from 20 keV to 6 MeV was observed in the computations. The initially injected current and accelerated current were 300 mA and 68.5 mA, respectively. The diameter and transverse emittance of the accelerated electron bunches were 0.18 mm and 1.51 mm mrad, respectively. Based on the computational design and physical analysis discussed in this paper, the 9.3 GHz 6 MeV side-coupled LINAC waveguide was fabricated and brazed successfully. The electric field distribution in the waveguide was measured by a bead-pull test. Consequently, without any mechanical tuning, it was compared with 3D simulation data and showed reasonable agreement.

Chapter 4

Generation of an electron micro-bunch train from a dc-biased ac-driven vacuum diode

The bunching frequency of electrons from an ac-driven vacuum diode has been studied by theory and simulation. And it can be increased unlimitedly to the terahertz (THz) region by widening the gap distance with the aid of a dc electric field. Specifically, a correlation between the bunching frequency and the transit phase (equivalently the transit time) of electrons was derived theoretically. The origin of the upper frequency limitation was explained by abnormal exclusion of a certain range of transit phase. The limitation has conventionally been believed to be imposed by the transit time effect. In a three-dimensional particle-in-cell simulation, a micro-bunch train with 1.41 picosecond periodicity (0.707 THz) was obtained from a gap of 50 μm . The results of simulation confirm our theoretical prediction that the bunching frequency can be significantly extended without suffering from the transit time effect.

4.1 Introduction

For the past years, the generation of an electron bunching with sub-picosecond periodicity has been a subject of great interest to its feasibility of being used for coherent terahertz (THz) radiation [41,42]. To produce such short-period micro-bunches, one popular method is using a photocathode with carefully manipulated laser pulses [43–45]. Activating spatial beam-wave interaction [41,46] or creating a virtual cathode in a diode [47,48] are also interesting ways to generate tunable micro-bunches.

The methods described above usually demand big acceleration facilities or fine control of laser systems, whereas the electron bunch train can also be generated simply by gating the electric field between the cathode and grid in a vacuum diode cavity (klystrode) [49–51], which has been used in the microwave region historically. Though lots of efforts have been devoted to extending the operation frequency of this device to tens of gigahertz (GHz) or sub-THz, no success has been achieved in breaking the upper barrier at a few GHz, due to the inherent upper frequency limitation given by the well-known *transit time effect*: as the operation frequency increases, some electrons return to the cathode surface or are decelerated by encountering the reversed electric field, which eventually blurs the bunching and weakens the intensity of the bunches.

Conventionally it has been believed that the transit time effect can be suppressed in a reduced gap, which ensures escaping of electrons by extricating them from the reversed field. In such a case, electrons may escape the gap before facing the reversed electric field. Reduction of the gap distance down to 1 μm demonstrated by the field emission arrays (FEAs) [52–55] seemed to be the best

solution to counteract the transit time effect. However, the modulation frequency of electron bunching has been strictly limited under tens of GHz, due to the large capacitance originating from short gap distances [43]. Though CNT (carbon nano tube)-based cold cathodes [56–58] enable significant reduction of the gap distance, the shortest periodicity of the electron bunch train ever demonstrated experimentally from a CNT cathode up to now is merely above 1.5 GHz [56], seemingly due to the transit time effect. While the transit time effect in vacuum diodes is regarded as a crucial factor to prohibit increasing the modulation frequency, the physical understanding of this phenomenon still remains at just an intuitive level or phenomenological from the experimental results.

In this paper, for the first time as far as we know, a fully quantitative, theoretical understanding of the transit time effect on the modulation frequency in a vacuum diode is provided, along with physical conditions to break that limit. Using the concept of excluded transit phase (ETP), we quantitatively explain why the upper frequency barrier had resided at around just a few GHz in the previous research [42,49–56,59]. ETP, which is one of the interesting phenomena we discovered theoretically in this work, means that a certain range of the transit phase can be wholly excluded, so that any micro-bunches emitted with ETP collapse before they reach the anode grid. Additionally, we reveal that the normally-believed demand for reduced gap distance to relax the transit time effect is a misguided constraint, by showing that spatial separation between bunches traversing a wide gap can be well preserved as long as the excluded transit phase is sufficiently suppressed by means of dc bias. Subsequently, from a three-dimensional particle-in-cell simulation, a train of well-separated micro-bunches with 1.41 picosecond periodicity (0.707 THz) could be obtained, perfectly matching the theoretical prediction, even for 50 μm -wide gap spacing, where a significant transit time effect had been expected.

4.2 Theory and numerical simulation

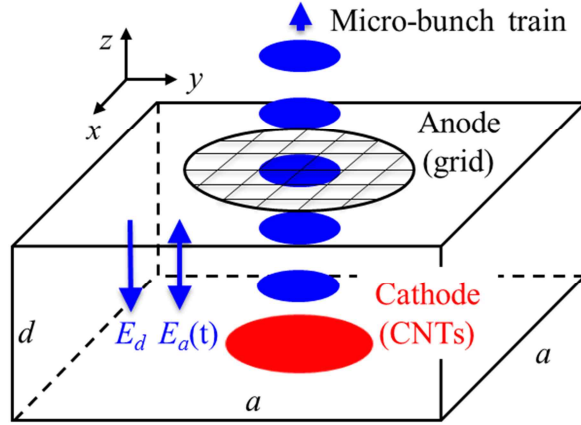


Figure 4.1: Schematics of the dc-biased, ac-driven vacuum diode cavity with a CNT cathode

The schematic of the dc-biased, ac-driven diode is presented in Fig. 4.1. The dc field is put in the negative z -direction between the top and bottom plates of the cavity. The parallel ac-field can be built-up resonantly, being fed from an external high-frequency power source. As a material for electron field emission, represented by a red circle at the center of the bottom plate, we assumed a CNT emitter. For the one-dimensional analysis of this system, the variation of the electric field in the x - and y -directions over the beam cross section is neglected. Since the actual shape of the cavity is not critical under this assumption, without loss of generality, we consider a rectangular cavity driven by the simplest TM_{110} mode, whose amplitude reaches its maximum at the center of the bottom plate.

For the TM_{110} mode, the z -directional electric field is uniform along the z -direction. Hence the total of ac and dc fields exerting on each electron can be written by

$$E_z(t) = -E_a \sin(\omega t + \phi) + E_d, \quad 0 \leq \phi < 2\pi, \quad (4.1)$$

where E_a , E_d , and ϕ represent the ac amplitude, dc field, and the initial phase of the emitted electron, respectively. Note that time t in Eq. (4.1) is referenced to each electron, so that it is emitted at $t = 0$ and sees the electric field $-E_a \sin\phi + E_d$ at the moment of the emission. Without loss of generality we confine E_a to be positive.

Under this electric field, the current density of the electrons yielded by the CNT emitter obeys the Fowler-Nordheim (FN) formula.

$$J_z(t) = \begin{cases} \frac{A\beta^2 E_z(t)^2}{\phi_\omega} \exp\left(\frac{-B\phi_\omega^{3/2}}{\beta|E_z(t)|}\right), & E_z(t) < 0 \\ 0, & E_z(t) \geq 0 \end{cases} \quad (4.2)$$

where β is the field enhancement factor and ϕ_ω is the work function. Since the electrons can be emitted only for a negative electric field, the negatively maximum electric field $-E_M$, which is determined by $-E_M = -E_a + E_d$ from Eq. (4.1), should be kept negative for a non-zero electron emission. Here we impose a couple of constraints on the ac and dc fields; first E_M should be smaller than the threshold of material breakdown of the CNT cathode. Simultaneously the ac and dc amplitudes are arranged so that the maximum field E_M is always kept fixed by a value as large as possible for the maximal extraction of electrons from the cathode. Under these constraints, as the dc field becomes negatively stronger, the temporal range for the electron emission increases as shown in Fig. 4.2.

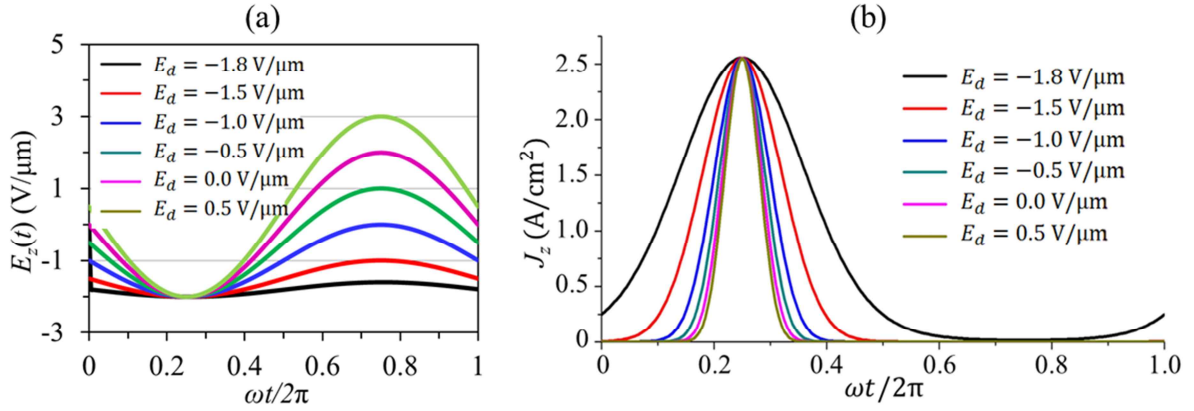


Figure 4.2: (a) Electric field obtained from Eq. (4.1) for various E_d . (b) Emitted beam current from CNT obtained from Fowler-Nordheim formula with $\beta=2.0 \times 10^3$, $\phi_\omega=5.0$ eV, $A=1.56 \times 10^{-6}$ AV^{-2}eV , $B=6.83 \times 10^9$ $\text{eV}^{-3/2}\text{Vm}^{-1}$ for various E_d .

To make the further analysis simple, we assume that every electron is emitted with zero velocity at $z = 0$. Neglecting the space charge effect for a low density beam, the electron trajectory becomes completely one-dimensional. To find the electron trajectory, we integrated the equation of motion with the electric field given by Eq. (4.1) for the initial condition given above. With normalization of the fields by

$$\bar{E}_d \equiv \frac{E_d}{E_M}, E_a = E_M(1 + \bar{E}_d), \quad (4.3)$$

we obtained

$$v_z(t) = \frac{eE_M}{m\omega} \left[\bar{E}_d \left\{ \cos\phi - \cos(\theta + \phi) + \theta \right\} - \cos(\theta + \phi) + \cos\phi \right] \quad (4.4)$$

$$z(t) = \frac{eE_M}{m\omega^2} \left[\bar{E}_d \left\{ \theta \cos\phi - \sin(\theta + \phi) - \frac{1}{2}\theta^2 + \sin\phi \right\} - \sin(\theta + \phi) + \theta \cos\phi + \sin\phi \right] \quad (4.5)$$

where $\theta = \omega t$.

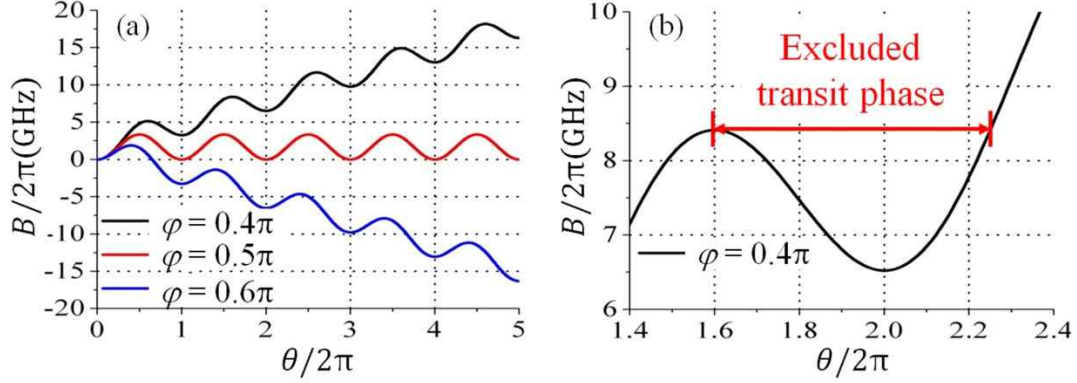


Figure 4.3: (a) Coefficient B in Eq. (7) for $E_d = 0$ for different ϕ 's. (b) Excluded transit phase (the arrowed region).

The most critical information obtainable from the trajectory equation (4.5) is the transit time for the electron to traverse the gap distance d for a given ac driving frequency. After traversing the gap, the electrons reach the upper plate and escape the system as an electron beam. The transit time can be obtained by equating the position $z(t)$ to the gap distance d to yield

$$\omega = A\bar{E}_d + B \quad (4.6)$$

along with

$$\begin{aligned}
 A &= \omega_0 \left[-\frac{\theta^2}{2} - \sin(\theta + \phi) + \theta \cos \phi + \sin \phi \right] \\
 B_n &= \omega_0 \left[-\sin(\theta + \phi) + \theta \cos \phi + \sin \phi \right]
 \end{aligned} \quad (4.7)$$

where $\omega_0 \equiv eE_M/\sqrt{2}\pi m dk$. In Eq. (4.7), we employed the cavity length ratio $k = d/a$, and used the relation between the resonance frequency and the cavity size a for the TM_{110} mode, described by $\omega = \sqrt{2}\pi c/a$. The physical meaning of Eq. (4.6) is that if a pair θ and ϕ exist to satisfy Eq. (4.6), for a given positive ac driving frequency ω , then the electron emitted with the initial phase ϕ can eventually reach the upper plate after transit time $t = \theta/\omega$. Considering that the electron emission occurs in a bunched form as implied by Fig. 4.2, the existence of such a solution to Eq. (4.6) indicates that an electron beam bunched by periodicity $2\pi/\omega$ can be extracted out of the cavity. Consequently the possibility of generating bunched beams can be exploited by analyzing the behavior of the coefficients A and B .

We first address the case of zero dc field, which was experimentally studied in a previous paper [56]. In this case the initial phase of an electron and its transit time to traverse the gap is determined only by the B coefficient. Figure 4.3 represents $B/2\pi$ as a function of θ for several different ϕ 's around $\phi/2$, where the electron emission is abundant (see Fig. 4.2). As typical values of E_M and k , we used 2×10^6 V/m and 0.025, respectively, which yield $\omega_0 = 1.05 \times 10^{10}$ (rad /s) in Eq. (4.7). What is predictable from this figure is, first, that there is an upper limit in the ac frequency with which the electrons can reach the upper plate to escape the cavity. For example, when the driving frequency is larger than 3.5 GHz, there is no solution to $\omega = B$ for $\phi \geq 0.5\pi$ (see Fig. 4.3), which means that half of the emitted electrons from the cathode cannot reach the upper plate in a finite time scale. Electrons with $\phi < 0.5\pi$, which are the other half of the emitted electrons, have a solution to Eq. (4.6) for an arbitrarily high ω . However in this case, the range of emitting phase ϕ of the electrons escaping the system is significantly limited by the *excluded transit phase* (ETP). ETP is an interesting phenomenon first introduced in this paper; once an electron reaches the upper plate to escape the cavity, it is not influenced by the applied field any more. Hence only the first crossing point of $y = \omega$ and $y = B$ is a meaningful solution of Eq. (4.6). Thus the crossing points located around the trough of the B -curve are actually excluded from the possible transit phase. Such an excluded phase is represented in Fig. 4.3 (b) by the arrowed region. Consequently, the beam charge becomes significantly small when the ac frequency is higher than a few GHz. As far as we know, this is the first theoretical understanding why the extraction of the bunched beam is not so efficient in the ac-only-driven system.

The limitation on the beam bunching frequency can be dramatically removed by adding a dc field in a negative direction. Due to the $-0.5 \theta^2$ term in coefficient A in Eq. (4.7), ω eventually becomes a monotonically increasing function of θ as \bar{E}_d increases. This indicates that, for any arbitrarily high driving frequency ω , we can find a proper transit phase θ satisfying Eq. (4.6) for any initial phase ϕ . Furthermore the ETP region can be wholly removed for a suitably high dc electric field. In other words, all the electrons emitted from the cathode can eventually escape the gap for any high frequency ω .

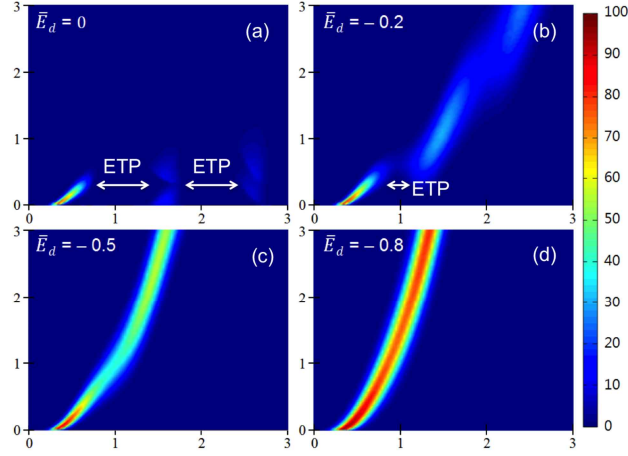


Figure 4.4: The map of bunching frequency ω and the final transit phase of electrons for different \bar{E}_d 's. (a) $\bar{E}_d = 0.0$, (b) $\bar{E}_d = -0.2$, (c) $\bar{E}_d = -0.5$, and (d) $\bar{E}_d = -1.0$

The correlations between the modulation frequency ω and the gap transit phase θ can be found in Fig. 4.4 for different values of \bar{E}_d . The x -coordinate represents the sum of the initial phase and the transit phase, $\phi + \theta$, normalized by 2π , and the y -coordinate represents the beam modulation frequency f normalized by ω_0 defined in Eq. (4.7). For this figure we numerically calculated the θ of thousands of sample electrons, varying ω . As the number of sample electrons with a given range of ϕ obeys Eq. (4.7), the x -directional width of continuous strips or discontinuous pieces corresponds to the bunch width in units of time normalized by a single ac period, and the color of the strips represents relative current density of the bunch. The color is scaled so that the current density is maximized at 100. When the dc field is zero, possible normalized frequency f/ω_0 is limited roughly under 2.0, corresponding to just a few GHz typically for $E_M \sim 2 \times 10^6$ V/m. The discontinuity of the permitted transit phase in this case can be understood by the ETP described above. As \bar{E}_d increases, the discontinuity vanishes and a continuous strip arises along with an increase of current density. As an example of an intermediate case between discontinuous pieces and a continuous strip, the case of $\bar{E}_d = -0.2$ is given in Fig. 4.4 (b). In that case, when f/ω_0 is chosen at around 0.5 or 2.0, an abrupt expansion of the phase width is expected, which implies blurring of the beam bunch. When \bar{E}_d is less than -0.5, the ETP disappears and a continuous strip begins to be clearly exposed with the increase of current density. Note that not only the disappearance of the ETP but also the increased number of electrons initially emitted from the cathode is the reason of the increased current density.

The cases with more extended parameters from Fig. 4.4 are presented in Fig. 4.5. Interestingly the width of the phase remains quite localized under a half-period even if the frequency enters far into the THz regime. Such collective motion of electrons implies that the normally-believed demand for

reducing the gap distance between the cathode and grid to minimize the transit time (or equivalently transit phase) for relaxing the transit time effect is a misguided constraint. Oppositely, widening of the gap distance accompanied by sufficient suppression of ETP by means of dc bias is an effective way to increase the modulation frequency ω , promisingly up to sub-THz or THz regimes. As shown in Fig. 4.5, the frequency corresponding to the transit phase increases more rapidly as \bar{E}_d approaches -1.0. Increasing of the phase width as \bar{E}_d approaches -1.0 can be easily deducible, because the extreme case of $\bar{E}_d = -1.0$ means that a continuous dc field is applied to the CNT cathode, which then emits the electrons without any modulation.

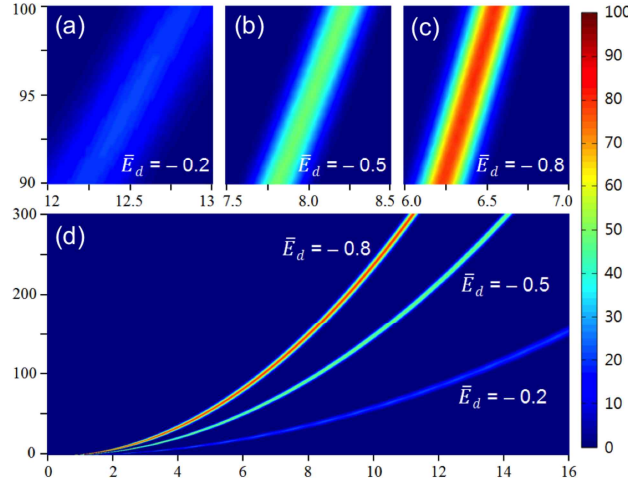


Figure 4.5: Map of ω vs. $\theta + \phi$, similar to Fig. 4.4, but for extended parameters, (a), (b), (c) with $\bar{E}_d = -0.2$, $\bar{E}_d = -0.5$, and $\bar{E}_d = -0.8$, respectively. (d) the map over the whole range.

Here we can find the condition for the excluded transit phase to wholly disappear for any value of θ by solving $\partial\omega/\partial\theta \leq 0$ in Eq. (4.6) to yield

$$\bar{E}_d \leq \frac{\cos(\theta + \phi) - \cos\phi}{-\theta - \cos(\theta + \phi) + \cos\phi} \equiv f(\theta, \phi). \quad (4.8)$$

From some simple algebra, it can be found that $f(\theta, \phi) \geq -0.5$ for any value of θ or ϕ . Thus $\bar{E}_d \leq -0.5$ is a universal condition for the deteriorating excluded transit phase to be wholly removed, and accordingly the bunched beam frequency can be increased unlimitedly. We note that this result is only for the case where the beam charge is low enough for the space charge effect to be neglected.

The analysis up to this point has been for space-charge-free cases. To secure the feasibility of the idea described above under more realistic conditions, we conducted a three-dimensional particle-in-cell simulation. The simulation parameters are set so that the electron beam is micro-bunched with a 707 GHz ac field. For this the transverse dimension of the cavity is set as $a = 300 \mu\text{m}$. The gap distance is $50 \mu\text{m}$ and the ac and dc amplitudes are $\pm 1.0 \times 10^6 \text{ V/m}$, respectively, which corresponds to $E_M = -2 \times 10^6 \text{ V/m}$ and $\bar{E}_d = -0.5$. In the PIC simulation, an analytic form for the TM_{110}

cavity mode is employed, but the self-generated field by the electrons is self-consistently calculated so that the space charge effect can be properly counted. Under these conditions, as shown in Fig. 4.6, a very nice micro-bunch train of emitted electrons is observed, showing the electron current of order 0.1 mA (see the inset), which is a remarkably high current density beam containing considerable space charge force. In principle, even a much higher amount of current can be acquired by using high order TM_{mn0} modes [75,76] instead of the fundamental TM_{110} mode which was dealt here for simplicity.

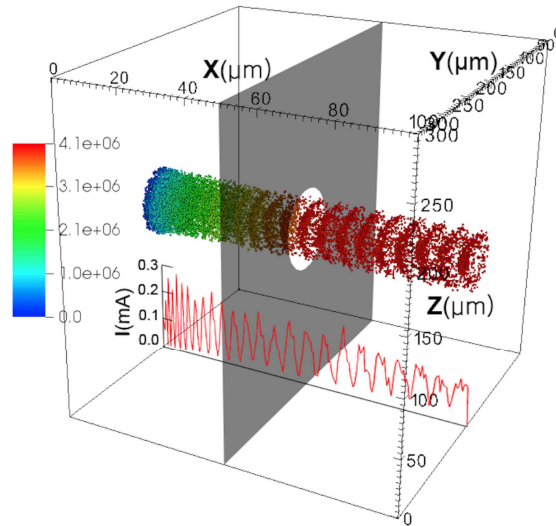


Figure 4.6: Three dimensional PIC simulation of the micro-bunching. The shaded plane marks the upper plane of the cavity. The three-dimensional plot was made via ViSit software [3]. The inset represents the electric current along the bunch train

4.3 Conclusion

In conclusion, we discovered theoretically that the normally-believed upper frequency barrier of an electron micro-bunch train from a vacuum diode can be broken through with the aid of dc-bias. Contrary to the conventional way to minimize the transit time effect by reducing the gap distance, we have shown that the gap should be widened with a proper dc electric field to increase the bunching frequency unlimitedly to the THz regime. This is a direct consequence of our theory, which reveals the correlation between the bunching frequency and the transit phase (or equivalently the transit time) taken by each electron to traverse the gap. Specifically we have shown that the electrons can move through the gap maintaining their bunch shape, even if their transit phases are larger than a multiple of 2π . In addition, we discovered that there exists an excluded transit phase (ETP) under a certain condition, making the electron bunches emitted with ETP be blurred out before they escape the diode. We found a condition of dc field to completely suppress the ETP. In a three-dimensional PIC simulation, a spatially well-localized micro-bunch train with 1.41 picosecond periodicity (0.707 THz) could be extracted from a vacuum diode with 50 μm gap distance, corresponding to a transit phase of

about ten times 2π . The simulation result verifies our theoretical prediction that the micro-bunching frequency of electrons from vacuum diodes can be extended significantly up to THz regimes by widening the gap with a proper dc field.

Chapter 5

Summary

In this thesis, I presented two topics of electron bunching in vacuum devices: electron gun, linear accelerator. For the electron gun, there are two different theoretical approaches of bunching condition in dc-biased ac-driven vacuum devices. The one is electron bunching from a DC-biased single surface multipactor. Generation of electron bunch from a dc biased, single surface multipactor was studied theoretically and by PIC simulations. The condition for a spatially narrow bunch was obtained and verified by PIC simulations. I extended our previous work to find the influences of much broader secondary emission spectrum and emission angle, which are always inherent in real materials. The broad secondary energy spectrum and emission angle effects influence the phase spread (or the longitudinal bunch size), sometimes broadening it or sometimes narrowing it down, depending on which of spectral broadening or peak shift is dominant. I also studied the case where the copper, whose secondary spectrum is even wider, was used as an emission plate. In this case also, the bunch size slightly decreased by the emission angle effect: the numerical value of the longitudinal bunch size for copper was $80\mu\text{m}$, which is suitable for the generation of THz wave generation. The other one is a theoretical correlation between the periodicity of an electron micro-bunch train and the transit phase of each electrons passing through a vacuum gap in a dc-biased ac-driven diode was derived. Contrary to the conventional way to minimize the transit time effect by reducing the gap distance, we have shown that the gap should be widened with a proper dc electric field to increase the bunching frequency unlimitedly to the THz regime. These kinds of bunched beam in condition of THz wave generation are proposed to be used as a compact electron gun for various applications, such as linear accelerators. For LINAC, computational design process for a 9.3 GHz (X-band) 6 MeV side-coupled LINAC waveguide has been developed. The design process contains 3D calculations of an entire structure of the LINAC waveguide. Based on the computational design and physical analysis discussed in this paper, the 9.3 GHz 6 MeV side-coupled LINAC waveguide was fabricated and brazed successfully. The electric field distribution in the waveguide was measured by a bead-pull test. Consequently, without any mechanical tuning, it was compared with 3D simulation data and showed reasonable agreement.

References

- [1] S.-G. Jeon, J.-I. Kim, S.-T. Han, S.-S. Jung, J.U. Kim, Theoretical study of dc-biased single-surface multipactors, *Phys. Plasmas*. 16 (2009).
- [2] M. Furman, M. Pivi, Technical Report SLAC-PUB-9912, LBNL-52807. (2003).
- [3] H. Childs, E. Brugger, A contract based system for large data visualization, *VIS 05. IEEE*. (2005).
- [4] M.S. Hur, J.-I. Kim, G.-J. Kim, S.-G. Jeon, Effects of the energy spread of secondary electrons in a dc-biased single-surface multipactor, *Phys. Plasmas*. 18 (2011).
- [5] E.F. Vance, One-Sided Multipactor Discharge Modes, *J. Appl. Phys.* 34 (1963).
- [6] H.C. Kim, J.P. Verboncoeur, Time-dependent physics of a single-surface multipactor discharge, *Phys. Plasmas*. 12 (2005).
- [7] R.A. Kishek, Y.Y. Lau, L.K. Ang, A. Valfells, R.M. Gilgenbach, Multipactor discharge on metals and dielectrics: Historical review and recent theories, *Phys. Plasmas*. 5 (1998).
- [8] M.H. Greenblatt, A Microwave Secondary Electron Multiplier, *Rev. Sci. Instrum.* 20 (1949).
- [9] S. Riyopoulos, Higher-order, asymmetric orbit multipactors, *Phys. Plasmas*. 14 (2007).
- [10] J.R.M. Vaughan, Multipactor, *IEEE Trans. Electron Devices*. 35 (1988) 1172–1180.
- [11] R. Kishek, Y.Y. Lau, Interaction of Multipactor Discharge and rf Circuit, *Phys. Rev. Lett.* 75 (1995) 1218–1221.
- [12] A. Frotnpour, G. Dadashzadeh, M. Shahabadi, B. Gimeno, Analysis of Multipactor RF Breakdown Thresholds in Elliptical Waveguides, *IEEE Trans. Electron Devices*. 58 (2011) 876–881.
- [13] C. Chang, G. Liu, C. Tang, C. Chen, J. Fang, Review of recent theories and experiments for improving high-power microwave window breakdown thresholds, *Phys. Plasmas*. 18 (2011) 055702.
- [14] L. Wu, L.K. Ang, Multipactor discharge in a dielectric-loaded accelerating structure, *Phys. Plasmas*. 14 (2007)
- [15] V. Semenov, V. Nechaev, E. Rakova, N. Zharova, D. Anderson, M. Lisak, et al., Multiphase regimes of single-surface multipactor, *Phys. Plasmas*. 12 (2005).
- [16] C.J. Karzmark, C.S. Nunan, E. Tanabe, *Medical electron accelerators*, McGraw-Hill, Incorporated, Health Professions Division, 1993.
- [17] Y. Kamino, K. Tsukuda, M. Kokubo, S. Miura, E. Hirai, M. Hiraoka, et al., Development of a new concept automatic frequency controller for an ultrasmall C-band linear accelerator guide, *Med Phys*. 34 (2007).
- [18] T.P. Wangler, *RF Linear accelerators*, John Wiley & Sons, 2008.
- [19] J. St. Aubin, S. Steciw, B.G. Fallone, The design of a simulated in-line side-coupled 6 MV linear accelerator waveguide, *Med Phys*. 37 (2010).

- [20] J. Shao, Y. Du, H. Zha, J. Shi, Q. Gao, Q. Jin, et al., Development of a C-band 6 MeV standing-wave linear accelerator, *Phys. Rev. Spec. Top. Beams*. 16 (2013) 90102.
- [21] M. Uesaka, T. Natsui, K. Lee, K. Dobashi, T. Yamamoto, T. Fujiwara, et al., 950keV, 3.95MeV and 6MeV X-band linacs for nondestructive evaluation and medicine, *Nucl. Instruments Methods Phys. Res. Sect. A Accel. Spectrometers, Detect. Assoc. Equip.* 657 (2011) 82–87.
- [22] K. Lee, E. Hashimoto, T. Yamamoto, T. Natsui, A. Mori, S. Hirai, et al., Design and experiment of dual-energy X-ray material recognition using a 950keV X-band Linac, *Nucl. Instruments Methods Phys. Res. Sect. A Accel. Spectrometers, Detect. Assoc. Equip.* 637 (2011) S54–S56.
- [23] C. Tang, H. Chen, Y. Liu, X. Wang, Low-energy linacs and their applications in Tsinghua University, in: *Proc. LINAC, 2006*: pp. 256–258.
- [24] C. Christou, X-band linac technology for a high repetition rate light source, *Nucl. Instruments Methods Phys. Res. Sect. A Accel. Spectrometers, Detect. Assoc. Equip.* 657 (2011) 13–21.
- [25] R. Bartolini, Beam dynamics optimisation of an X-band Linac driven soft X-ray FEL, *Nucl. Instruments Methods Phys. Res. Sect. A Accel. Spectrometers, Detect. Assoc. Equip.* 657 (2011) 177–181.
- [26] P. Gouard, S. Champeaux, P. Liger, D. Morisseau, G.-L. Calhène, SIMULATION OF AN INDUSTRIAL LINAC (5 MeV, 1 mA, 3 GHz) WITH MAGIC® ELECTROMAGNETIC PIC CODE, (2010).
- [27] Y. Kamino, K. Takayama, M. Kokubo, Y. Narita, E. Hirai, N. Kawawda, et al., Development of a four-dimensional image-guided radiotherapy system with a gimbaled X-ray head, *Int. J. Radiat. Oncol. Biol. Phys.* 66 (2006) 271–278.
- [28] Y. Kamino, S. Miura, M. Kokubo, I. Yamashita, E. Hirai, M. Hiraoka, et al., Development of an ultrasmall C-band linear accelerator guide for a four-dimensional image-guided radiotherapy system with a gimbaled x-ray head, *Med Phys.* 34 (2007) 1797–1808.
- [29] T. Depuydt, D. Verellen, O. Haas, T. Gevaert, N. Linthout, M. Duchateau, et al., Geometric accuracy of a novel gimbals based radiation therapy tumor tracking system, *Radiother. Oncol.* 98 (2011) 365–372.
- [30] H. Yang, S.H. Kim, J. Jang, S.J. Park, M.H. Cho, W. Namkung, et al., Design of Compact C-band Standing-wave Accelerating structure Enhancing RF Phase Focusing, in: *Proc. of IPAC12, 2012*: pp. 20–25.
- [31] H.R. Yang, S.H. Kim, S.J. Park, M.H. Cho, W. Namkung, J.S. Oh, Self-focusing Effects in Compact C-band Standing-wave Accelerating Structure for X-ray Imaging Applications, *Proc. of IPAC11*. (2011) 4–9.
- [32] S.H. Kim, H.R. Yang, S.I. Moon, J. Jang, Y.M. Gil, M. Cho, et al., Cold test on C-band standing-wave accelerator, in: *Part. Accel. Conf. 2007. PAC. IEEE, IEEE, 2007*: pp. 2823–2825.
- [33] B. Wei, X. Zhou, J. Xiao, L. Ming, Physical design and cooling test of C-band standing wave accelerating tube, *Chinese Phys.* 15 (2006) 319.
- [34] T. Yamamoto, T. Natsui, F. Sakamoto, M. Uesaka, N. Nakamura, E. Tanabe, DEVELOPMENT OF PORTABLE X-BAND LINAC X-RAY SOURCE FOR NON-DESTRUCTIVE TESTING, in: *Jt. Int. Work. Nucl. Technol. Soc. – Needs Next Gener.*, n.d.
- [35] J. Gonichon, D. Tronc, Acceleration and bunching in a 6 MV X band linac, in: *1996 Eur. Part. Accel. Conf. Sitges, Spain, 1996*.

- [36] J.R. Adler Jr, S.D. Chang, M.J. Murphy, J. Doty, P. Geis, S.L. Hancock, The Cyberknife: a frameless robotic system for radiosurgery, *Stereotact Funct Neurosurg.* 69 (1997) 124–128.
- [37] J.S. Aubin, S. Steciw, C. Kirkby, B.G. Fallone, An integrated 6 MV linear accelerator model from electron gun to dose in a water tank, *Med Phys.* 37 (2010) 2279–2288.
- [38] A.A. Zavadtsev, A.A. Krasnov, I.S. Kuzmin, N.P. Sobenin, A.I. Fadin, Accelerating Structure of 10 MeV Electron Linac, *Proceeding of RUPAC.* (2004).
- [39] K. Halbach, R.F. Holsinger, SUPERFISH—a computer program for evaluation of RF cavities with cylindrical symmetry, *Part. Accel.* 7 (1976) 213–222.
- [40] C.S.T.M. Studio, Computer Simulation Technology, GmbH, Darmstadt, Ger. (2009).
- [41] S. Antipov, M. Babzien, C. Jing, M. Fedurin, W. Gai, A. Kanareykin, et al., Subpicosecond Bunch Train Production for a Tunable mJ Level THz Source, *Phys. Rev. Lett.* 111 (2013) 134802.
- [42] S. Seletskiy, B. Podobedov, Y. Shen, X. Yang, Seeding, Controlling, and Benefiting from the Microbunching Instability, *Phys. Rev. Lett.* 111 (2013) 034803.
- [43] L. Hudanski, E. Minoux, L. Gangloff, K.B.K. Teo, J.-P. Schnell, S. Xavier, et al., Carbon nanotube based photocathodes., *Nanotechnology.* 19 (2008) 105201.
- [44] Y. Li, K.-J. Kim, Nonrelativistic electron bunch train for coherently enhanced terahertz radiation sources, *Appl. Phys. Lett.* 92 (2008) 014101.
- [45] J.G. Neumann, R.B. Fiorito, P.G. O’Shea, H. Loos, B. Sheehy, Y. Shen, et al., Terahertz laser modulation of electron beams, *J. Appl. Phys.* 105 (2009) 053304.
- [46] S. Bielawski, C. Evain, T. Hara, M. Hosaka, M. Katoh, S. Kimura, et al., Tunable narrowband terahertz emission from mastered laser–electron beam interaction, *Nat. Phys.* 4 (2008) 390–393.
- [47] A. Pedersen, A. Manolescu, Á. Valfells, Space-Charge Modulation in Vacuum Microdiodes at THz Frequencies, *Phys. Rev. Lett.* 104 (2010) 175002.
- [48] P. Jonsson, M. Ilkov, A. Manolescu, A. Pedersen, A. Valfells, Tunability of the terahertz space-charge modulation in a vacuum microdiode, *Phys. Plasmas.* 20 (2013) 023107.
- [49] A.V. Haeff, L.S. Nergaard, A Wide-Band Inductive-Output Amplifier, *Proc. IRE.* 28 (1940) 126–130. doi:10.1109/JRPROC.1940.228986.
- [50] A.J. Lichtenberg, Prebunched beam traveling-wave tube studies, *IRE Trans. Electron Devices.* 9 (1962) 345–351.
- [51] D.H. Preist, M.B. Shrader, The klystrode—An unusual transmitting tube with potential for UHF-TV, *Proc. IEEE.* 70 (1982) 1318–1325.
- [52] J.P. Calame, H.F. Gray, J.L. Shaw, Analysis and design of microwave amplifiers employing field-emitter arrays, *J. Appl. Phys.* 73 (1993) 1485.
- [53] K.L. Jensen, Field emitter arrays for plasma and microwave source applications, *Phys. Plasmas.* 6 (1999) 2241.
- [54] C.A. Spindt, C.M. Armstrong, C.R. Smith, B.M. Gannon, D.R. Whaley, Application of field emitter arrays to microwave power amplifiers, *IEEE Trans. Plasma Sci.* 28 (2000) 727–747.

- [55] S. Tsujino, M. Paraliiev, E. Kirk, C. Gough, S. Ivkovic, H.-H. Braun, Sub-nanosecond switching and acceleration to relativistic energies of field emission electron bunches from metallic nano-tips, *Phys. Plasmas*. 18 (2011)
- [56] K.B.K. Teo, E. Minoux, L. Hudanski, F. Peauger, J.-P. Schnell, L. Gangloff, et al., Microwave devices: carbon nanotubes as cold cathodes., *Nature*. 437 (2005) 968.
- [57] A.G. Rinzler, J.H. Hafner, P. Nikolaev, P. Nordlander, D.T. Colbert, R.E. Smalley, et al., Unraveling nanotubes: field emission from an atomic wire., *Science*. 269 (1995) 1550–3.
- [58] W.A. de Heer, A. Ch telain, D. Ugarte, A Carbon Nanotube Field-Emission Electron Source, *Science* (80-.). 270 (1995) 1179–1180.
- [59] F.M. Charbonnier, J.P. Barbour, L.F. Garrett, W.P. Dyke, Basic and applied studies of field emission at microwave frequencies, *Proc. IEEE*. 51 (1963) 991–1004.
- [60] C.K.. Birdsall, A. Langdon, *Plasma physics via computer simulation*, (1985).
- [61] M. Furman, M. Pivi, Probabilistic model for the simulation of secondary electron emission, *Phys. Rev. Spec. Top. - Accel. Beams*. 5 (2002) 124404.
- [62] G. Cheng, L. Liu, Monte Carlo modeling of secondary electron emission and its incorporation in particle simulations of electron–surface interaction, *Comput. Phys. Commun*. 182 (2011) 1295–1303.
- [63] SLAC renamed to SLAC Natl. Accelerator Laboratory, *Stanford Dly.* (2008).
- [64] Stanford Linear Accelerator Center renamed SLAC National Accelerator Laboratory, *SLAC National Accelerator Laboratory*, 2008.
- [65] D. Davino, *Theory, Design and Tests on a Prototype Module of a Compact Linear Accelerator for Hadrontherapy*, (2000).
- [66] E. Tanabe, Voltage breakdown in S-band linear accelerator cavities, *Nucl. Sci. IEEE Trans.* 30 (1983) 3551–3553.
- [67] W.D. Kilpatrick, Criterion for vacuum sparking designed to include both rf and dc, *Rev. Sci. Instrum.* 28 (1957) 824–826.
- [68] E. Tanabe, Voltage Breakdown in S-Band Linear Accelerator Cavities, *IEEE Trans. Nucl. Sci.* 30 (1983) 3551–3553.
- [69] Y. Kamino, S. Miura, M. Kokubo, I. Yamashita, E. Hirai, M. Hiraoka, et al., Development of an ultrasmall C-band linear accelerator guide for a four-dimensional image-guided radiotherapy system with a gimbaled x-ray head., *Med. Phys.* 34 (2007) 1797–808.
- [70] X. Xu, R.S. Callin, W.R. Fowkes, A. Menegat, G.P. Scheitrum, D.H. Whittum, RF breakdown studies in X-band klystron cavities, in: *Proc. 1997 Part. Accel. Conf. (Cat. No.97CH36167)*, IEEE, 1997: pp. 3045–3047.
- [71] SLAC-PUB-10175 -- Effect of RF Parameters on Breakdown Limits in High-Vacuum X-Band Structures, (n.d.).
- [72] R. Roy, O. Shanker, Calculation of intercavity coupling coefficient for side coupled standing wave linear accelerator, *IEEE Trans. Microw. Theory Tech.* 41 (1993) 1233–1235.

- [73] D. Alesini, A. Falone, M. Migliorati, A. Mostacci, F. Palpini, L. Palumbo, et al., Design and RF measurements of an X-band accelerating structure for linearizing the longitudinal emittance at SPARC, Nucl. Instruments Methods Phys. Res. Sect. A Accel. Spectrometers, Detect. Assoc. Equip. 554 (2005) 1–12.
- [74] L.C. Maier, J.C. Slater, Field Strength Measurements in Resonant Cavities, J. Appl. Phys. 23 (1952) 68–77. .
- [75] S.-G. Jeon, Y.-M. Shin, K.-H. Jang, S.-T. Han, J.-K. So, Y.-D. Joo, et al., High order mode formation of externally coupled hybrid photonic-band-gap cavity, Appl. Phys. Lett. 90 (2007) 021112.
- [76] K.-H. Jang, S.-G. Jeon, J.-I. Kim, J.-H. Won, J.-K. So, S.-H. Bak, et al., High order mode oscillation in a terahertz photonic-band-gap multibeam reflex klystron, Appl. Phys. Lett. 93 (2008) 211104.

APPENDIX

Physical constants

Speed of light	c	2.99792458×10^8 m/s
Elementary charge	e	$1.60217733 \times 10^{-19}$ C
Electron mass	m_e	$0.510\,999\,06$ MeV/ c^2
Proton mass	m_p	$938.272\,31$ MeV/ c^2
Atomic mass unit *	m_u	$931.494\,32$ MeV/ c^2
Permeability of free space	μ_0	$4\pi \times 10^{-7}$ T-m/A
Permittivity of free space	ϵ_0	$1/\mu_0 c^2 = 8.85487817 \dots \times 10^{-12}$ F/m
DC resistivity of copper (293 K)	$1/\sigma$	1.7×10^{-8} Ω -m (nominal)

